Durham Research Online

Deposited in DRO:

14 November 2017

Version of attached file:

Published Version

Peer-review status of attached file:

Peer-reviewed

Citation for published item:

Further information on publisher's website:

Publisher's copyright statement:

The evolution of the star formation rate function in the EAGLE simulations: a comparison with UV, IR and Hα observations from $z \sim 8$ to $z \sim 0$

A. Katsianis,[1][⋆] G. Blanc,[1,2] C. P. Lagos,[3] N. Tejos,[4] R. G. Bower,[5] A. Alavi,[6] V. Gonzalez,[1] T. Theuns,[5] M. Schaller[5] and S. Lopez[1]

[1]*Department of Astronomy, Universität de Chile, Camino El Observatorio 1515, Las Condes, Santiago, Chile*
[2]*Observatories of the Carnegie Institution for Science, Pasadena, CA 91101, USA*
[3]*International Centre for Radio Astronomy Research (ICRAR), M468, University of Western Australia, 35 Stirling Hwy, Crawley, WA 6009, Australia*
[4]*Instituto de Física, Pontificia Universidad Católica de Valparaíso, Casilla 4059, Valparaíso, Chile*
[5]*Institute for Computational Cosmology, Department of Physics, University of Durham, South Road, Durham DH1 3LE, UK*
[6]*Department of Physics and Astronomy, University of California, Riverside, CA 92521, USA*

ABSTRACT

We investigate the evolution of the galaxy star formation rate function (SFRF) and cosmic star formation rate density (CSFRD) of $z \sim 0$–8 galaxies in the Evolution and Assembly of GaLaxies and their Environments (EAGLE) simulations. In addition, we present a compilation of ultraviolet, infrared and H α SFRFs and compare these with the predictions from the EAGLE suite of cosmological hydrodynamic simulations. We find that the constraints implied by different indicators are inconsistent with each other for the highest star-forming objects at $z < 2$, a problem that is possibly related to selection biases and the uncertainties of dust attenuation effects. EAGLE's feedback parameters were calibrated to reproduce realistic galaxy sizes and stellar masses at $z = 0.1$. In this work we test if and why those choices yield realistic star formation rates (SFRs) for $z \sim 0$–8 as well. We demonstrate that supernovae feedback plays a major role at setting the abundance of galaxies at all star-forming regimes, especially at high redshifts. On the contrary, active galactic nuclei (AGN) feedback becomes more prominent at lower redshifts and is a major mechanism that affects only the highest star-forming systems. Furthermore, we find that galaxies with SFR $\sim$1–10 M$_\odot$ yr^{-1} dominate the CSFRD at redshifts $z \leq 5$, while rare high star-forming galaxies (SFR $\sim$10–100 M$_\odot$ yr^{-1}) contribute significantly only briefly around the peak era ($z \sim 2$) and then are quenched by AGN feedback. In the absence of this prescription objects with SFR $\sim$10–100 M$_\odot$ yr^{-1} would dominate the CSFRD, while the cosmic budget of star formation would be extremely high. Finally, we demonstrate that the majority of the cosmic star formation occurs in relatively rare high-mass haloes ($M_{\mathrm{Halo}} \sim 10^{11-13}$ M$_\odot$) even at the earliest epochs.

Key words: methods: numerical – galaxies: evolution – galaxies: formation – galaxies: luminosity function, mass function – galaxies: star formation – cosmology: theory.

1 INTRODUCTION

Within the last decade, large galaxy surveys have allowed us to obtain good insight for a range of properties of galaxies [e.g. stellar masses, star formation rates (SFRs), metallicities, circular velocities] in a wide redshift range. These provided us with further understanding on how galaxies evolve, allowing us to constrain theoretical models and simulations. The observed number density of

star-forming galaxies as a function of their SFR, namely the star formation rate function (SFRF) can give further comparisons with numerical results. The SFR, unlike the stellar mass that is a cumulative property, represents an instantaneous census of star formation. Physical mechanisms [e.g. supernovae (SNe) and active galactic nuclei (AGN) feedback] affect the SFRs of the simulated objects the moment they become prominent. This makes the SFRF an ideal and sensitive test for studying various physical prescriptions.

Galaxy formation and evolution is a complex process that involves various astrophysical phenomena, such as the non-linear evolution of dark matter haloes, gas cooling, feedback and star

⋆E-mail: kataunichile@gmail.com, kata@das.uchile.cl

formation. Theoretical studies of the evolution of the SFRF and cosmic star formation rate density (CSFRD) require detailed modelling. The above have been investigated both by semi-analytic models (Fontanot et al. 2012; Gruppioni et al. 2015) and hydrodynamic simulations (Davé, Oppenheimer & Finlator 2011; Tescari et al. 2014; Katsianis et al. 2017). Typically, the comparison of the models with observations suggested that simulations overproduce galaxies of all kinds of SFRs. According to the authors, the tension with observables could be due to the fact that there was not an implementation of AGN feedback in their models. Tescari et al. (2014) and Katsianis et al. (2017) studied the role of feedback from SNe and AGN in the evolution of the SFRF of $z \sim 1$–7 galaxies using the set of cosmological hydrodynamic simulations, AustraliaN GADGET-3 early Universe Simulations (ANGUS). The authors found that a key factor for reproducing the observed distribution of SFRs is the presence of SNe feedback that is prominent at high redshifts ($z \geq 4$) and become less efficient with time. Gruppioni et al. (2015) compared predictions of state-of-the-art semi-analytic models of galaxy formation and evolution (e.g. Monaco, Fontanot & Taffoni 2007; Henriques et al. 2015) with observations of the PACS Evolutionary Probe survey and Herschel Multi-tiered Extragalactic Survey data sets in the Cosmological Evolution Survey (COSMOS) and Great Observatories Origins Deep Survey (GOODS)-South fields. The comparison showed that semi-analytic models underpredict the bright end of the SFRF at $z \geq 2$. According to the authors the cause of this underprediction could be due to improper numerical implementation of AGN or stellar feedback that may be too efficient for the bright star-forming objects in the models.

The Virgo project Evolution and Assembly of GaLaxies and their Environments (EAGLE) simulations (Crain et al. 2015; Schaye et al. 2015) is a suite of cosmological hydrodynamical simulations in cubic, periodic volumes ranging from 25 to 100 comoving Mpc per side. They track the evolution of baryonic gas, stars, massive black holes (BHs) and non-baryonic dark matter particles from a starting redshift of $z = 127$ down to $z = 0$. The different runs were performed to investigate the effects of resolution, box size and various physical prescriptions (e.g. feedback and metal cooling). The EAGLE reference simulation has 2×1504^3 particles (an equal number of gas and dark matter elements) in an $L = 100$ comoving Mpc volume box, initial gas particle mass of $m_g = 1.81 \times 10^6 \, M_\odot$ and mass of dark matter particles of $m_g = 9.70 \times 10^6 \, M_\odot$. It is one of the highest resolution cosmological hydrodynamic simulations ran in such a large volume (Vogelsberger et al. 2014; Schaye et al. 2015). It has been calibrated to reproduce observational data sets, such as the present-day stellar mass function of galaxies, the correlation between the BH and masses and the dependence of galaxy sizes on mass. Alongside with these key properties, the simulation was able to match many other observed properties of galaxies at various eras, like molecular hydrogen abundances (Lagos et al. 2015), colours and luminosities at $z \sim 0.1$ (Trayford et al. 2015), supermassive black hole (SMBH) mass function (Rosas-Guevara et al. 2016), angular momentum evolution (Lagos et al. 2017), atomic hydrogen abundances (Crain et al. 2017) and sizes (Furlong et al. 2017). Therefore the EAGLE simulations can provide a powerful resource for understanding the SFRs of galaxies and their evolution across cosmic time. In addition, the SFRF was not used to tune the models, so it can be seen as an independent test for the predictions from the simulations.

In this paper we use the EAGLE cosmological suite of simulations to study the evolution of the SFRF and CSFRD at $z \sim 0$–8. In Section 2 we present the compilation of the observed luminosity functions (LFs) and dust correction laws used for this work

alongside with the methodology employed to obtain the galaxy SFRFs.[1] In Section 3 we present a brief description of the EAGLE simulations along with the subgrid model used to describe star formation. In Section 4 we compare the simulated EAGLE SFRFs and CSFRD with the constraints from the observations.[2] In Section 5 we investigate the contribution of haloes with different masses to the SFRF and CSFRD. In Section 6 we present the SNe and AGN feedback implementations in EAGLE and explore their effect on the simulated SFRF. Finally, in Section 7 we summarize our main results and conclusions.

2 THE OBSERVED STAR FORMATION RATES FROM GALAXY LUMINOSITIES

There has been a considerable effort to estimate the SFRF and CSFRD in the literature (Ménard et al. 2011; Smit et al. 2012; Madau & Dickinson 2014; Katsianis et al. 2017). Different groups typically rely on the observed luminosities and LFs with the commonly tracers being the ultraviolet (UV), Hα and infrared (IR) luminosities. Evolutionary synthesis models provide the relations between the SFR per unit mass, luminosity and the integrated colour of the population. For the case of the UV luminosity the relation to SFR (Kennicutt 1998b) is found to be

$$\text{SFR}_{\text{UV}} \, (M_\odot \, \text{yr}^{-1}) = 0.77 \times 10^{-28} \, L_{\text{UV}} \, (\text{erg s}^{-1} \, \text{Hz}^{-1}), \quad (1)$$

where L_{UV} is the UV luminosity of galaxies. The relation is valid from 1500 to 2800 Å and assumes a Chabrier (2003) initial mass function (IMF).[3] A disadvantage of UV light is that it is subject to dust attenuation effects and thus dust corrections are necessary to obtain the intrinsic luminosities, which can then be used to estimate the intrinsic SFRs (Smit et al. 2012). UV LFs usually provide information for a large number of galaxies at redshifts $z > 2$. At lower redshifts UV samples give key constraints only for low and intermediate star-forming objects (Katsianis et al. 2017). However, there are other tracers that provide information about dusty, high star-forming systems. For example, the IR luminosity originating from dust continuum emission is a star formation indicator that at the same time is a good test of dust physics (Hirashita, Buat & Inoue 2003). The relation between the SFR and total IR luminosity from the evolutionary synthesis model of Kennicutt (1998a) is found to be

$$\text{SFR}_{\text{IR}} \, (M_\odot \, \text{yr}^{-1}) = 10^{-10} \, L_{\text{IR}} \, /L_\odot, \quad (2)$$

where L_{IR} is the IR luminosity integrated between 8 and 1100 µm of galaxies assuming a Chabrier (2003) IMF. IR light is typically used to estimate obscured star formation, however, small galaxies with low metallicities do not have enough dust to reprocess the UV light to IR, so IR LFs do not probe the faint end of the SFRF, a problem that is quite notable and proportional to redshift (Katsianis et al. 2017). IR light is usually employed as a probe of the dust corrections that have to be used in the observed dust-attenuated UV luminosities. However, it has been discussed in the literature that IR calibrations may overestimate the SFRs of galaxies and the dust corrections they imply for UV light (e.g. Elbaz et al. 2010; Bauer et al. 2011; Papovich et al. 2011; Fumagalli et al. 2014; Hayward et al. 2014; Utomo et al. 2014; Katsianis, Tescari & Wyithe 2016).

---

[1] In Appendix A we present detailed tables of these constraints.

[2] In Appendix B we focus on the effects of resolution and box size.

[3] Originally the conversion reported by Kennicutt (1998a) assumed a Salpeter (1955) IMF, which produced 1.8 higher SFRs.

Some of the main reasons for overestimating the SFR measured from IR light could be the following.

(i) Buried AGN that boosts the IR luminosity.

(ii) Dust can be heated by old populations not related to recent star formation.

(iii) Converting the IR luminosity into SFR relies on assumptions that possibly do not hold for all galaxies. For example, the IR luminosity can overestimate the instantaneous SFR during the post-starburst phase by up to two orders of magnitude (Hayward et al. 2014). Even though the instantaneous SFR decreases rapidly after the starburst, the stars that were formed in the starburst can remain dust obscured and thus produce a significant IR luminosity not related to new born stars.

(iv) Larger polycyclic aromatic hydrocarbons emission of distant galaxies in 24 µm observations.

The ongoing *Herschel* mission is able to sample the IR peak and total IR-spectral energy distribution (SED) of numerous galaxy spectra, helping to derive more accurate L_{IR} values, thus the above problems could be diminished in the near future.

In addition to UV and IR light, H α photons, which are produced from the gas ionized by the radiation of young and massive stars can be used to trace the intrinsic SFR of an object (Hanish et al. 2006; Bell et al. 2007; Ly et al. 2011; Sobral et al. 2013). According to the synthesis models of Kennicutt (1998a), the relation between SFR and H α luminosity is

$$\mathrm{SFR}_{\mathrm{H}\alpha} \; (\mathrm{M}_\odot \; \mathrm{yr}^{-1}) = 4.4 \times 10^{-42} \; L_{\mathrm{H}\alpha} \; (\mathrm{erg \; s}^{-1}), \tag{3}$$

where $L_{\mathrm{H}\alpha}$ is the H α luminosity of the galaxies and conversion assumes a Chabrier (2003) IMF. H α light is subject to dust attenuation effects so dust corrections are necessary to calculate the intrinsic SFR of the target (Hopkins et al. 2001; Sobral et al. 2013; An et al. 2014). We note that all the above methods that employ the UV, IR and H α luminosities to measure star formation do not measure instantaneous SFRs, but instead, measure the time-averaged quantity. The different luminosities have their origins in stars of different masses and differences between the different tracers are expected (Lee et al. 2009). For example, H α traces very massive stars, while UV is tracing lower mass stars ($\sim 3 \, \mathrm{M}_\odot$). IR light can be even more troublesome as it depends on the dust abundance and composition of the target. Because of the above problems a 50 per cent systematic uncertainty in the calibrations given in equations (1)–(3) can be expected.

To construct the SFRFs for redshift $z \sim 8.0$ to $z \sim 0$ we use a range of UV, IR, H α and radio LFs. We do so since this combination enable us to study the SFRF in a large range of SFRs and redshifts. In addition, we employ the SFRFs presented by Smit et al. (2012, $z \sim 4$–7), Duncan et al. (2014, $z \sim 4$–7) and Katsianis et al. (2017, $z \sim 1$–4).

UV light is subject to dust-attenuation effects. We follow the method described in Smit et al. (2012) and Katsianis et al. (2017) to correct the UV luminosity bins of the UV LF. Like Smit et al. (2012), we assume the infrared excess (IRX)–β relation of Meurer, Heckman & Calzetti (1999):

$$A_{1600} = 4.43 + 1.99 \, \beta, \tag{4}$$

where A_{1600} is the dust absorption at 1600 Å and β is the UV continuum spectral slope. We assume a linear relation between β and the luminosity (Bouwens et al. 2012):

$$\langle \beta \rangle = \frac{\mathrm{d}\beta}{\mathrm{d}M_{\mathrm{UV}}} \left(M_{\mathrm{UV,AB}} + 19.5 \right) + \beta_{M_{\mathrm{UV}} = -19.5}. \tag{5}$$

Then, following Hao et al. (2011) we assume

$$L_{\mathrm{UV_{OBS}}} = L_{\mathrm{UV_{corr}}} \, \mathrm{e}^{-\tau_{\mathrm{UV}}}, \tag{6}$$

where τ_{UV} is the effective optical depth ($\tau_{\mathrm{UV}} = A_{1600}/1.086$). H α emission is also subject to dust-attenuation effects. Sobral et al. (2013) used a 1 mag correction at the bins of the LF, while Ly et al. (2011) use the SFR-dependent dust correction suggested by Hopkins et al. (2001). We present the results of both authors.

Finally to obtain the intrinsic SFRFs we convert the luminosity bins of the dust-corrected LFs and the Kennicutt relations (equations 1–3). We present these distributions alongside with the EAGLE reference SFRFs in Figs 1 and 2. Tables presenting these determinations can be found in Appendix A.

3 STAR FORMATION IN THE EAGLE SIMULATIONS

In this section we present an overview of the EAGLE set of simulations and how star formation is implemented. The cosmological parameters assumed in all runs are those reported by the Planck Collaboration I (2014); Planck Collaboration XVI (2014) with the average densities of matter, dark energy and baryonic matter in units of the critical density at redshift 0 being $\Omega_{\mathrm{m}} = 0.307$, $\Omega_{\lambda} = 0.693$ and $\Omega_{\mathrm{b}} = 0.04825$, respectively, Hubble parameter $h = H_0/100 \, \mathrm{km \, s}^{-1} \, \mathrm{Mpc}^{-1} = 0.6777$, square root of the linear variance of the matter distribution $\sigma_8 = 0.8288$, scalar power-law index of the power spectrum of primordial adiabatic perturbations $n_{\mathrm{s}} = 0.9611$ and primordial abundance of helium $Y = 0.248$. The initial conditions were generated using the transfer function of the CAMB software (Lewis et al. 2000) and the perturbation theory as described by Jenkins (2013). The simulations were run using an improved and updated version of the *N*-body TREEPM smoothed particle hydrodynamics code GADGET-3 (Springel 2005). The subgrid routines that describe subgrid physics like star formation and stellar mass loss are updated versions of those used for the Galaxies–Intergalactic Medium Interaction Calculation (GIMIC; Crain et al. 2009), OverWhelmingly Large Simulations (OWLS; Schaye et al. 2010) and cosmo-OWLS (Le Brun et al. 2014) projects. In this study we focus on 'intermediate-resolution simulations' (as labelled by Schaye et al. 2015) using volumes of side $L = 25$, 50 and 100 Mpc. We also use low-resolution and high-resolution runs with different box sizes to address the effects of resolution and volume. In Table 1 we present the EAGLE simulations used for this work.

Star formation occurs in cold ($T \leq 10^4$ K), high-density gas. Cosmological simulations, at present, lack the resolution and the detailed physics to model the cold, interstellar phase. To overcome this limitation, EAGLE employs the star formation recipe of Schaye & Dalla Vecchia (2008). In this scheme, gas with densities exceeding the critical density for the onset of the thermogravitational instability ($n_{\mathrm{H}} \sim 10^{-2}$–$10^{-1}$ cm^{-3}) is treated as a multiphase mixture of cold molecular clouds, warm atomic gas and hot ionized bubbles that are all approximately in pressure equilibrium (Schaye 2004). The above mixture is modelled using a polytropic equation of state $P = k\rho^{\gamma_{\mathrm{eos}}}$, where P is the gas pressure, ρ is the gas density and k is a constant that is normalized to $P/k = 10^3$ cm^{-3} K at the density threshold $n_{\mathrm{H}}^\star$ that marks the onset of star formation. The hydrogen number density, n_{H}, is related to the overall gas density, ρ, via $n_{\mathrm{H}} = X\rho/m_{\mathrm{H}}$, where X is the hydrogen mass fraction ($X = 0.752$) and m_{H} is the mass of a hydrogen atom. The threshold $n_{\mathrm{H}}^\star$ was set as 0.1 cm^{-3} in the OWLS simulations in accordance with theoretical considerations (Schaye & Dalla Vecchia 2008) and is comparable with other work in the literature (Springel & Hernquist 2003;

Table 1. Summary of the different EAGLE simulations used in this work. Column 1: run name; column 2: box size of the simulation in comoving Mpc; column 3: total number of particles ($N_{TOT} = N_{GAS} + N_{DM}$ with $N_{GAS} = N_{DM}$); column 4: mass of the dark matter particles; column 5: initial mass of the gas particles; column 6: comoving gravitational softening length; column 7: resolution with respect the reference L100N1504-Ref run (higher ratios correspond to higher resolution); column 8: combination of feedback implemented. The L25N752-Recal run is a configuration in which the feedback prescriptions are recalibrated to obtain the observed galaxy stellar mass function at $z \sim 0$. The run is employed to test the convergence of the EAGLE simulations.

Run	L (Mpc)	N_{TOT}	m_{DM} ($M_\odot$)	m_{GAS} ($M_\odot$)	ϵ_{com} (kpc)	Resolution (Ref)	Feedback
L100N1504-Ref	100	2×1504^3	9.70×10^6	1.81×10^6	2.66	1.0	AGN + SNe
L50N752-Ref	50	2×752^3	9.70×10^6	1.81×10^6	2.66	1.0	AGN + SNe
L50N752-NoAGN	50	2×752^3	9.70×10^6	1.81×10^6	2.66	1.0	No AGN + SNe
L25N376-Ref	25	2×376^3	9.70×10^6	1.81×10^6	2.66	1.0	AGN + SNe
L25N376-WeakSNfb	25	2×376^3	9.70×10^6	1.81×10^6	2.66	1.0	AGN + weak SNe
L25N376-StrongSNfb	25	2×376^3	9.70×10^6	1.81×10^6	2.66	1.0	AGN + strong SNe
L25N752-Ref	25	2×752^3	1.21×10^6	2.26×10^5	1.33	8.0	AGN + SNe
L25N188-Ref	25	2×188^3	7.76×10^7	1.45×10^7	5.32	0.125	AGN + SNe
L25N752-Recal	25	2×752^3	1.21×10^6	2.26×10^5	1.33	8.0	AGN + SNe Recal

Vogelsberger et al. 2013). In addition to the above density-dependent criterion, the star formation model employed in this work takes into account that the transition from the warm phase to the cold occurs more efficiently in metal-rich environments. Thus, EAGLE simulations adopt the metallicity-dependent star formation threshold proposed in Schaye (2004), which is

$$n_H^\star(Z) = 0.1 \text{ cm}^{-3} \left(\frac{Z}{0.002} \right)^{-0.64}, \tag{7}$$

where Z is the gas metallicity. Besides the density threshold, gas has to fulfil the requirement of being cold. Following Dalla Vecchia & Schaye (2012), gas is eligible to form stars if its temperature $\log_{10} T \leq \log_{10} T_{crit} = \log_{10} T_{eos} + 0.5$, where T_{eos} is the temperature floor and fulfil the metallicity-dependent density criterion described by equation (7). Finally, to prevent star formation in low-overdensity gas at high redshift, there is an additional criterion for star-forming gas to have an overdensity $\delta > 57.7$.

After the above criteria determine which gas particles are eligible to be star forming the Schaye & Dalla Vecchia (2008) scheme employ the observed Kennicutt–Schmidt low (Schmidt 1959; Kennicutt 1998a) to describe star formation. Under the assumption that the gas is self-gravitating the Kennicutt–Schmidt star-forming law can be written as

$$\dot{\Sigma}_\star = A \left(\frac{\Sigma_g}{1 \, M_\odot \, \text{pc}^{-2}} \right)^n, \tag{8}$$

where $\Sigma_\star$ and Σ_g are the surface density of stars and gas, respectively. Assuming a polytropic equation of state, equation (8) can be rewritten in a pressure-dependent form:

$$\dot{m}_\star = m_g \, A \, (1 \, M_\odot \, \text{pc}^{-2})^{-n} \left(\frac{\gamma}{G} \, f_g \, P \right)^{(n-1)/2}, \tag{9}$$

where m_g is the mass of the gas particle for which we are computing $\dot{m}_\star$, $n = 1.4$, $A = 1.515 \times 10^{-4} \dot{m}_\star$ yr^{-1} kpc^{-2}, $\gamma = 5/3$ is the ratio of specific heats for a monoatomic gas, G is the gravitational constant, f_g is the mass fraction in gas and P is the total pressure.

Equations (7) and (9) define the algorithm to calculate the rate at which gas is converted into stars. Star particles are to be interpreted as simple stellar populations (SSP, i.e. an assembly of coeval, initially chemically homogeneous single stars) with an initial mass, age and chemical composition originating from its progenitor gas particle following a Chabrier (2003) IMF in the range 0.1–100 $M_\odot$.

The stellar evolution and chemical enrichment are described in Wiersma et al. (2009). We follow the metal recycling by massive stars (Type II SNe, stellar winds), intermediate-mass stars (Type Ia SNe) and asymptotic giant branch (AGB) stars of the 11 elements that contribute significantly to the radiative cooling rates using the nucleosynthetic yields from Portinari, Chiosi & Bressan (1998) and Marigo (2001). At each time step and for each stellar particle, the stellar mass reaching the end of the main-sequence phase is identified using the metallicity-dependent lifetimes of Portinari et al. (1998).

In this work, galaxies and their host haloes are identified by a friends-of-friends (FoF) algorithm (Davis et al. 1985) followed by the SUBFIND algorithm (Springel, Yoshida & White 2001; Dolag & Stasyszyn 2009) that is used to identify substructures or subhaloes across the simulation. The SFR of each galaxy is defined to be the sum of the SFR of all gas particles that belong to the corresponding subhalo and that are within a 3D aperture with radius 30 kpc (Crain et al. 2015; Schaye et al. 2015).

4 THE EVOLUTION OF THE SIMULATED AND OBSERVED STAR FORMATION RATES

4.1 The evolution of the star formation rate function

In this section we present the evolution of the SFRF of the EAGLE reference model alongside with constraints from observations. At high redshifts ($z \gtrsim 4$) usually only the UV emission from galaxies is observable with the available instrumentation. Thus, the SFRFs at high redshifts rely mostly on UV-selected samples in the literature. For example, Smit et al. (2012) used the Kennicutt (1998a) UV–SFR conversion and the luminosity-dependent dust corrections of Meurer et al. (1999) to transform the UV LFs of Bouwens et al. (2007, $z \sim 4$–6) and Bouwens et al. (2011, $z \sim 7$) into SFRFs. The dark green crosses of Fig. 1 represent the results described above. The dark green triangles of Fig. 1 represent the SFRFs of Duncan et al. (2014), which were obtained following the SED fitting technique (Bruzual & Charlot 2003; Röllig et al. 2013). In addition, we use the UV LFs from Bouwens et al. (2015, $z \sim 4$–10) and the dust corrections described in Section 2. The dark green filled diamonds of Fig. 1 show these results. Bouwens et al. (2015) combined the CANDELS, HUDF0–9, HUDF1–2, ERS and BoRG/HIPPIES programs to map the evolution of the UV LF. The updated LF determinations reach
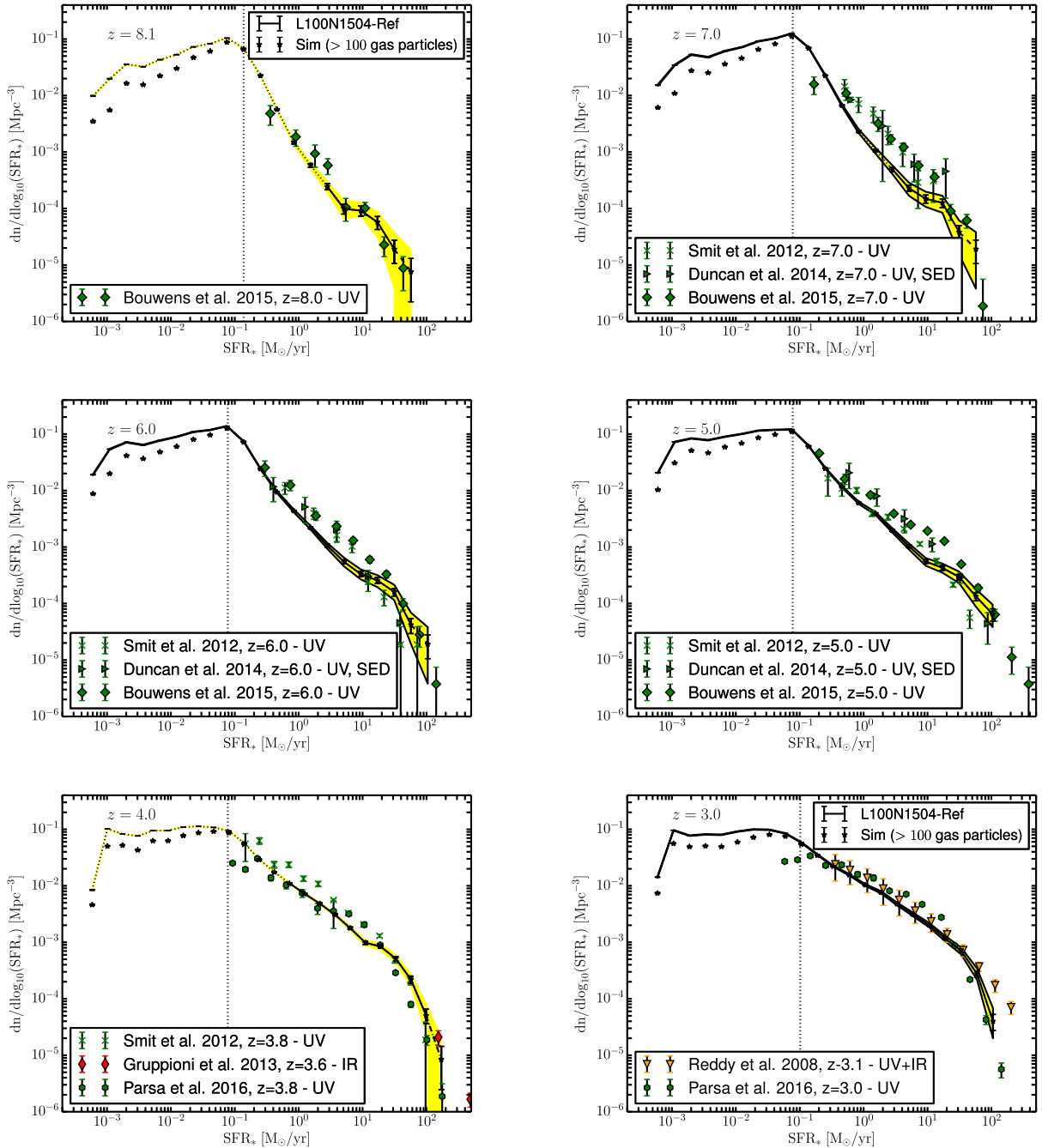
Figure 1. Comparison between the L100N1504-Ref SFRF (black dashed line) and observations for redshifts $z \sim 8.0$ (top left-hand panel), $z \sim 7.0$ (top right-hand panel), $z \sim 6.0$ (middle left-hand panel), $z \sim 5.0$ (middle right-hand panel), $z \sim 4.0$ (bottom left-hand panel) and $z \sim 3.0$ (bottom right-hand panel). For all observations a Chabrier (2003) IMF and ΛCDM cosmology same as EAGLE is assumed. Dark green crosses were taken from the work of Smit et al. (2012). The dark green triangles represent the results of Duncan et al. (2014). We note that an uncertainty of 50 per cent in the Kennicutt calibrations could lead the estimates for the observed SFR to move left or right in the plots by ∼0.3 dex. In Appendix A we present detailed tables of the constraints we obtained using UV, IR and Hα LFs. The yellow area represents the 95 per cent bootstrap confidence interval for 1000 resamples of the EAGLE SFRs, while the black error bars represent the 1σ Poissonian errors. Following the convention by Schaye et al. (2015) when a bin of the EAGLE SFRF contains objects with stellar masses below the mass limit of 100 (initial mass, m_{GAS}) baryonic particles curves are dotted, when there are fewer than 10 galaxies curves are dashed. To describe the limits due to poor sampling of gas particles we present the SFRF of objects that contain more than 100 gas particles (black stars+vertical dotted line). We see that at high redshifts the EAGLE SFRF can give insights mainly for intermediate and high star-forming objects.

lower magnitudes ∼− 16 AB mag and agree well with previous estimates. However, the larger samples and volumes give a more reliable sampling, especially at the characteristic luminosity $L^\star$.

Starting from redshift $z \sim 8$ (top left-hand panel of Fig. 1) we present a comparison between the L100N1504-Ref and the con-

straints implied by the Bouwens et al. (2015, $z \sim 8$,) data. The yellow area represents the 95 per cent bootstrap confidence interval for 1000 resamples of the SFR of the simulated galaxies, while the black error bars represent the Poissonian errors. To describe the limits due to poor sampling of gas particles we present the
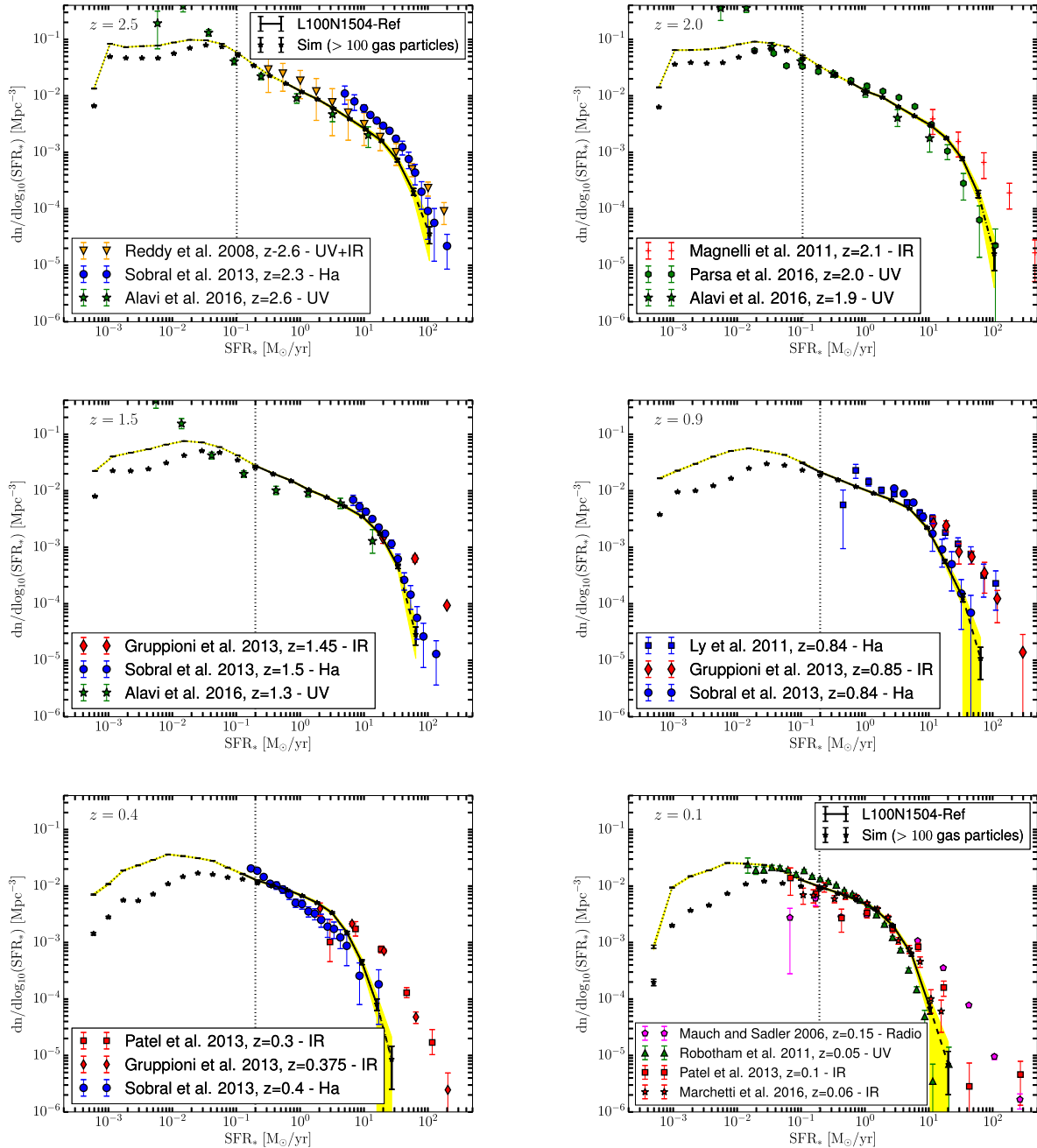
Figure 2. Comparison between the L100N1504-Ref SFRF (black dashed line) and observations for redshifts $z \sim 2.5$ (top left-hand panel), $z \sim 2.0$ (top right-hand panel), $z \sim 1.5$ (middle left-hand panel), $z \sim 0.85$ (middle right-hand panel), $z \sim 0.35$ (bottom left-hand panel) and $z \sim 0.1$ (bottom right-hand panel). In Appendix A we present detailed tables of the constraints we obtained using UV, IR and Hα LFs (see also Katsianis et al. 2017). The yellow area represents the 95 per cent bootstrap confidence interval for 1000 resamples of the EAGLE SFRs, while the black error bars represent the Poissonian errors. When a bin of the EAGLE SFRF contains objects with stellar masses below the mass limit of 100 baryonic particles curves are dotted, when there are fewer than 10 galaxies curves are dashed. To describe the limits due to poor sampling of gas particles we present the SFRF of objects that contain more than 100 gas particles (black stars+vertical dotted line).

SFRF of objects that contain more than 100 gas particles (black stars+vertical dotted line). In addition, when a bin of the EAGLE SFRF contains objects with stellar masses below the mass limit of 100 (initial mass, m_{GAS}) baryonic particles curves are dotted since sampling effects associated with limited resolution become important below this regime (Schaye et al. 2015). The agreement is quite good despite the above problems and the fact that most of the simulated galaxies at this high redshift suffer from resolution effects.

At $z \sim 7.0$ (top right-hand panel) we show that L00N1504-Ref is underproducing the number of objects with intermediate SFRs ($1 < \mathrm{SFR} < 10\,\mathrm{M_\odot\,yr^{-1}}$) but this could be due to limits of resolution that still look prominent. The picture is similar at $z \sim 6.0$ (middle left-hand panel of Fig. 1) and at $z \sim 5.0$ (middle right-hand panel of Fig. 1), where the L100N1504-Ref run is able to describe a larger range of the SFRF free of resolution and box size effects. At these high redshifts we see a slight underproduction by 0.2 dex

at the number density of objects with $1 < \mathrm{SFR} < 10\,\mathrm{M}_\odot\,\mathrm{yr}^{-1}$. Besides resolution effects, it is possible that the above is due to the strong SN feedback employed in the EAGLE reference model. We will see in detail the effect of both SN and AGN feedback prescriptions at various redshifts in Section 6. At $z \sim 4$ (bottom left-hand panel of Fig. 1) we see that UV studies (Smit et al. 2012; Parsa et al. 2016) are able to probe successfully galaxies with low ($0.1 < \mathrm{SFR} < 1\,\mathrm{M}_\odot\,\mathrm{yr}^{-1}$), intermediate ($1 < \mathrm{SFR} < 10\,\mathrm{M}_\odot\,\mathrm{yr}^{-1}$) and high ($10 < \mathrm{SFR} < 100\,\mathrm{M}_\odot\,\mathrm{yr}^{-1}$) SFRs. On the other hand, IR studies (Gruppioni et al. 2013) are limited to constrain only high star-forming systems ($\mathrm{SFR} > 100\,\mathrm{M}_\odot\,\mathrm{yr}^{-1}$) for this era. This can be due to the following reasons:

(i) different tracers possibly trace completely different population of galaxies and give only conditional SFRFs that do not represent the overall population;

(ii) intermediate and low SFR objects do not have enough dust to reprocess a large number of UV photons into the IR, thus IR surveys are unable to probe the faint-end slope of the distribution at early times;

(iii) mid-FIR surveys have limitations of resolution and surface brightness;

(iv) different indicators of SFR correspond to different time averages (e.g. IR measurements represent less instantaneous measurements than UV and Hα tracers).

At $z \sim 3.0$ (bottom right-hand panel of Fig. 1) we present a comparison between the reference model and the SFRFs obtained by Katsianis et al. (2017), which rely on the LFs determinations of Reddy et al. (2008, bolometric) and Parsa et al. (2016, UV-selected). We see that the two distributions are in good agreement, except for objects with $\mathrm{SFR} > 100\,\mathrm{M}_\odot\,\mathrm{yr}^{-1}$. With respect to the Reddy et al. (2008, bolometric) data, the EAGLE reference model slightly underpredicts the number density of high star-forming objects. On the other hand, the L100N1504-Ref run slightly overpredicts the number density of high star-forming galaxies with respect to the SFRF that relied on Parsa et al. (2016, UV) results.

To determine the SFRF at $z \sim 2.5$ (top left-hand panel of Fig. 2), we employ the bolometric LF of Reddy et al. (2008), the Hα data of Sobral et al. (2013) and the UV-selected LF of Alavi et al. (2016). Alavi et al. (2016) obtained near-UV imaging of three lensing clusters to study the evolution of the faint end of the UV LF. The L100N1504-Ref is broadly consistent with the constraints from observations. The different indicators provide SFRFs that are in agreement up to this redshift ($z \sim 2.5$). On the other hand, at redshift $z \sim 2.0$ (top right-hand panel of 2) we see that the SFRFs obtained from UV-selected samples (Alavi et al. 2016; Parsa et al. 2016) are not consistent with the constraints from the IR data (Magnelli et al. 2013) for galaxies with $\mathrm{SFR} \geq 80\,\mathrm{M}_\odot\,\mathrm{yr}^{-1}$. This tension can be due to the following reasons:

(i) dust corrections for UV luminosities (and especially those implied by the IRX–β relation) are uncertain for highly star-forming systems and possibly underestimated;

(ii) UV LFs are usually incomplete at the bright end of the distribution since bright objects have high dust contents and thus are invisible to UV surveys;

(iii) the SFR measured from IR light can be overestimated (see more details in Section 3).

The L100N1504-Ref SFRF at $z \sim 2.0$ generally lay between UV and IR constraints, but typically are closer to the UV SFRFs. However, we note that usually the highest star-forming bins contain less than 10 galaxies at most redshifts, thus the statistics are poor.

Simulations with larger box size and resolution are needed to have more meaningful comparisons in the high and low star-forming ends of the SFRF.

At $z \sim 1.5$ (middle left-hand panel of Fig. 2) we employ the IR LF of Gruppioni et al. (2013, $z \sim 1.45$), the Hα data of Sobral et al. (2013, $z \sim 1.5$) and the UV LF of Alavi et al. (2016, $z \sim 1.3$). Hα light is subject to dust attenuation effects. Thus, Sobral et al. (2013) applied a 1 mag correction across all bins of the observed Hα distribution to estimate a dust-free LF. Hopkins et al. (2001) noted that a more sophisticated luminosity-dependent dust correction law produces similar to 1 mag correction but only for local galaxies. Hopkins et al. (2001) suggest that at higher redshifts ($z > 0.3$), the 1 mag correction is possibly underestimating the dust corrections for objects with high luminosities. Thus, it is possible that the 1 mag correction to the Hα luminosities employed by Sobral et al. (2013) is underestimated resulting artificially in low SFRs at the high star-forming end. The L100N1504-Ref run is in agreement with the Hα and UV SFRFs but is underproducing the number density of objects with respect to IR constraints. We will see in more detail in Section 6.2 that the tension between the EAGLE reference model and the IR data could be due to the presence of the strong AGN feedback that is implemented. At $z \sim 0.8$ (middle right-hand panel of 2), we compare the reference model with the SFRFs reported by Katsianis et al. (2017) that rely on the Hα LFs of Ly et al. (2011) and Sobral et al. (2013) and the IR LF of Gruppioni et al. (2013). Ly et al. (2011) obtained measurements of the Hα LF for galaxies at $z \sim 0.8$, based on the NewHα Survey. In contrast to Sobral et al. (2013) who applied the 1 mag correction to their LF, Ly et al. (2011) adopted the luminosity-dependent extinction relation of Hopkins et al. (2001). Sobral et al. (2013) found that their results are in excellent agreement with Ly et al. (2011) if the authors assume the same dust corrections thus any differences between the Hα SFRFs present in the top panel of Fig. 2 are possibly due to differences in the treatment of dust. At $z \sim 0.4$ (bottom left-hand panel of Fig. 2) we see again that SFRFs that rely on IR studies imply a higher number density of high SFRs than the Hα LF of Sobral et al. (2013). The L100N1504-Ref model is in agreement with the SFRFs obtained using Sobral et al. (2013) data but underproduces the number density of objects when compared to IR studies by an order of magnitude at $\mathrm{SFR} > 100\,\mathrm{M}_\odot\,\mathrm{yr}^{-1}$. Finally, the reference model at $z \sim 0$ is in good agreement with the IR SFRF that rely on Marchetti et al. (2016). However, it underpredicts the number density of high star-forming compared to constraints from the radio observations of Mauch & Sadler (2007)[4] and the IR data of Patel et al. (2013). On the other hand, the EAGLE SFRF slightly overpredicts the number of high star-forming objects with respect the SFRF that rely on the near-UV (NUV) LF of Robotham et al. (2011).

In conclusion, we find that the EAGLE SFRF at $z \sim 0$–8 is consistent with the constraints from the observations, especially with those implied by UV and Hα studies, at the regimes where simulations are considered free from resolution and volume effects. There is a slight underproduction of objects with $\mathrm{SFR} \sim 1$–$10\,\mathrm{M}_\odot\,\mathrm{yr}^{-1}$ in the L0100N1504-Ref run with respect to the observations from all star formation indicators at $z \geq 3$. In addition, the simulation underpredicts the number of objects at the high star-forming end ($\mathrm{SFR} \sim 10$–$100\,\mathrm{M}_\odot\,\mathrm{yr}^{-1}$) with respect to IR and radio data for ≤ 2. We will see in Section 4.2 that objects at these regimes dominate the

---

[4] We use the calibration given by Sullivan et al. (2001) that suggests that the relation between SFR and radio luminosity is $\mathrm{SFR} = \frac{L_{\mathrm{radio}}}{8.85 \times 10^{20}}$. We convert the results for a Chabrier IMF by dividing them by 1.8.
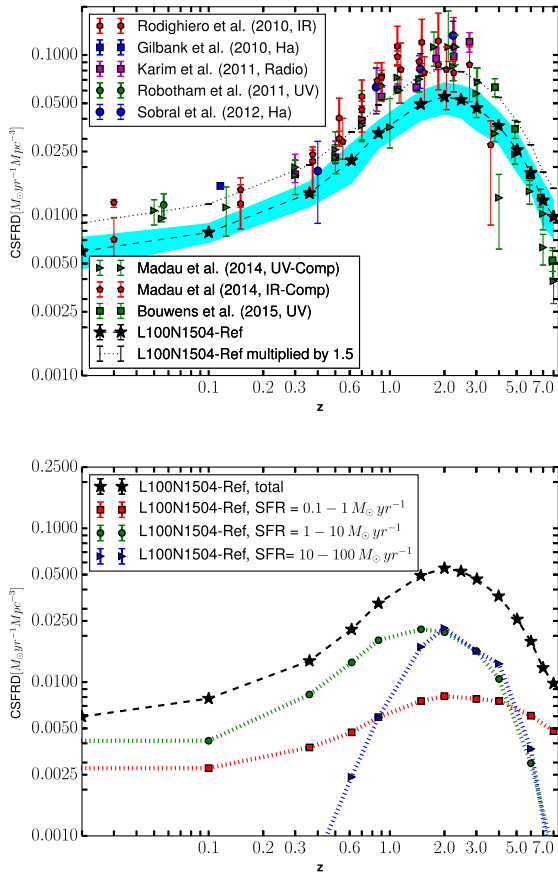
Figure 3. Top panel: the evolution of the EAGLE L100N1504-Ref CSFRD (black dashed line) of the Universe alongside with the observations of Madau & Dickinson (2014). The cyan region represents the cosmic variance due to the limited box size of the simulation (Driver & Robotham 2010). Bottom panel: the contribution of galaxies with different SFRs in the EAGLE CSFRD. Galaxies with low SFRs (SFR ~ 0.1–$1\,M_\odot\,yr^{-1}$) dominate the CSFRD at $z > 6$. The contribution of SFR ~ 10–$100\,M_\odot\,yr^{-1}$ is significant down to $z \sim 2$, below which it drops quickly. Galaxies with intermediate SFR ~ 1–$10\,M_\odot\,yr^{-1}$ dominate the CSFRD for most of the history of the Universe.

CSFRD, thus small disagreements between observed and simulated SFRFs for these galaxies may be responsible for disagreements between the EAGLE and observed CSFRDs.

4.2 The evolution of the cosmic star formation rate density

A standard way to describe the evolution of the SFR of the Universe as a whole is by providing estimates of the CSFRD at various redshifts. These are obtained usually by integrating LFs or SFRFs (Madau & Dickinson 2014; Katsianis et al. 2017) and give useful constraints on the theory and simulations. In the top panel of Fig. 3 we plot the CSFRD as a function of redshift for the L100N1504-Ref run alongside with the observations of Rodighiero et al. (2010, IR), Karim et al. (2011, radio), Sobral et al. (2013, Hα), Madau & Dickinson (2014, compilation) and Bouwens et al. (2015, UV). We use these measurements because when combined they can trace the evolution of the CSFRD for various redshifts and at the same time they represent results from different indicators giving a sense of systematic scatter. The dark green triangles of Fig. 3 and labelled as Madau & Dickinson (2014, UV-comp) represent a compilation

of UV observations (Schiminovich et al. 2005; Wyder et al. 2005; Dahlen et al. 2007; Reddy & Steidel 2009; Robotham et al. 2011; Bouwens et al. 2012; Cucciati et al. 2012). The red pentagons of Fig. 3 and labelled as Madau & Dickinson (2014, IR-comp) represent a compilation of IR observations (Sanders et al. 2003; Takeuchi, Yoshikawa & Ishii 2003; Magnelli et al. 2011, 2013; Gruppioni et al. 2013). The blue squares represent the results from the Hα study of Gilbank et al. (2010). The dark green circles were taken from Robotham et al. (2011). We see that estimates of the CSFRD from different indicators have an offset of around 0.2 dex but are broadly consistent.

Katsianis et al. (2017) compared measurements of the CSFRD obtained from the integration of UV, IR and Hα SFRFs at $z \sim 1$–4. The authors reported that different SFR indicators produce results consistent for the CSFRD, despite their differences (see also Section 4). This is possibly due to the fact that all SFRFs regardless of SFR tracer agree well for objects with intermediate SFRs (SFR ~ 1–$10\,M_\odot\,yr^{-1}$), which dominate the CSFRD at most redshifts (bottom panel of Fig. 3). However, we note that the measurements from IR data are found to be typically 0.10–0.25 dex higher. This may be due to the following reasons:

(i) the faint-end slopes of the IR SFRFs/LFs are not directly constrained by individually detected sources and rely only on extrapolations that usually have artificially smaller negative slope α;

(ii) the characteristic luminosity/SFR of IR LFs/SFRFs is typically higher than that of UV and Hα studies, which are unable to trace dusty systems with high SFRs.

In the top panel of Fig. 3 we see that the EAGLE CSFRD increases with time and peaks at $z \sim 2$. That era is followed by a constant decrement so that the CSFRD is almost 10 times lower by $z \sim 0$. As Furlong et al. (2015) pointed out this behaviour agrees well with the observed one but the L100N1504-Ref run has typically a normalization ~ 1.5 times lower than the observations. In the bottom panel of Fig. 3 we present the contribution of galaxies with different SFRs to the CSFRD in EAGLE. We see that galaxies with SFR ~ 1–$10\,M_\odot\,yr^{-1}$ have the largest contribution from redshift $z \sim 5$ and below. In addition, the high star-forming objects (SFR ~ 10–$100\,M_\odot\,yr^{-1}$) also make a large contribution at $z \sim 1.5$–5 but after that era they are suddenly quenched. In Section 4.1, where we presented the evolution of the SFRF, we showed that the number of the objects at both regimes is low with respect low star-forming objects at all redshifts. However, in this section we see that when combined they dominate the CSFRD. In Section 4.1 we also demonstrated that the EAGLE SFRF is typically lower by ~ 0.1 dex compared to the observations from various tracers for objects with SFR ~ 1–$10\,M_\odot\,yr^{-1}$ at $z \geq 3$. In addition, there is a tension of 0.1–1 dex with the IR data at the high star-forming end for $z \leq 2.0$. Since the above objects (bottom panel of Fig. 3) dominate the CSFRD, any disagreements between the simulated and observed SFRFs at these regimes can lead to disagreements between the simulated and observed CSFRDs as well.

The feedback mechanisms employed in the L100N1504-Ref run are responsible for suppressing the SFRs of these galaxies. This would have the effect of decreasing the simulated CSFRD and cause the tension between the model and the observations. However, we note that it is also possible that the observations of the CSFRD that mostly rely on the Kennicutt (1998a) conversion laws are overestimated (Katsianis et al. 2016). New calibrations with lower normalizations have been suggested in the literature (Otí-Floranes & Mas-Hesse 2010; Kennicutt & Evans 2012; Chang et al. 2015). For example, Chang et al. (2015) added

complementary data using *Herschel* observations to estimate SFRs and stellar masses. These measurements included dust emission and contamination from quiescent galaxies with the derived SFR–luminosity calibrations for 12 and 22 μm being 0.10–0.20 dex lower than previous measurements. In addition, we have to keep in mind that selection effects and biases definitely affect the measurements, since usually the UV and H α LFs are incomplete above the characteristic SFR and IR measurements rely on uncertain extrapolations for low-mass objects (see Section 4). We demonstrate that the contribution of low SFR galaxies (SFR ∼ 0.1–1 $M_\odot$ yr^{-1}) at most redshifts to the CSFRD is small. Any disagreements between our comparisons most likely arise from objects with higher SFR. We stress that the L100N1504-Ref run may suffer from resolution effects for low star-forming objects and their contribution could be higher in a simulation with higher resolution. Nevertheless, in Section 4.1 we showed that even at this limit observations and simulations of the SFRF are in excellent agreement.

Finally, we investigate which objects drive the peak of the CS-FRD. We see that besides objects with SFR ∼ 1–10 $M_\odot$ yr^{-1} the peak of the CSFRD at z ∼ 2 in the L100N1504-Ref is driven by the strong contribution of rare high star-forming galaxies (SFR ∼ 10–100 $M_\odot$ yr^{-1}). Their abundance and contribution decreases significantly and sharply after that epoch (bottom panel of Fig. 3). We note that the behaviour described above is not in agreement with the evolution implied by IR studies (e.g. Magnelli et al. 2013), at which the contribution of galaxies with high SFRs/luminosities to the CSFRD/total IR luminosity decreases much flatter. This discrepancy reflects the tension between the SFRFs of the EAGLE reference model and IR constraints. The later imply larger number densities of objects with SFR ∼ 10–100 $M_\odot$ yr^{-1} (Section 4.1) at z < 2, and the disagreement with the L100N1504-Ref run increases with time. In Section 6 we will see the important role that feedback plays on keeping the number of these extremely high star-forming objects low at these redshifts.

5 THE CONTRIBUTION OF HALOES WITH DIFFERENT MASSES TO THE SFRF AND CSFRD

In this section we present the contribution of haloes with various masses to the CSFRD (Fig. 4), the number density of haloes of different masses at different redshifts (Fig. 5) and their contribution on the SFRF (Fig. 6) in the EAGLE L100N1504-Ref run.
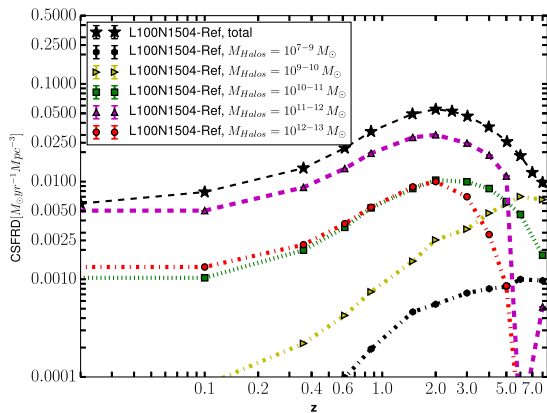

Figure 4. CSFRD contribution of haloes with different masses in EAGLE. Below redshift 5 objects with masses $M_{halo} = 10^{11-12}$ $M_\odot$ dominate through their high efficiencies besides their low numbers (Fig. 5).

Behroozi, Wechsler & Conroy (2013) and Moster, Naab & White (2013) argued that haloes near 10^{12} $M_\odot$ are the most efficient at forming stars at all redshifts with the baryon conversion efficiency ($M_\star/M_{baryon}$) dropping rapidly at both higher and lower masses. In addition, the stellar to halo mass ratio also peaks at 10^{12} $M_\odot$ (Behroozi et al. 2013). However, in the paradigm of hierarchical structure formation, small haloes form earlier than larger ones, which need some time to emerge. In Fig. 4 we see that at z ≥ 5 the CSFRD is dominated by relatively small haloes of mass $M_{halo} = 10^{9-10}$ $M_\odot$.[5] The left-hand panel of Fig. 5 reveals that the number of objects of this mass interval is high. In addition, the right-hand panel of the same figure, where we present the percentage of star-forming haloes at different masses (i.e. $n_{haloes, SFR > 0}/n_{haloes, total}$), shows that a large percentage (>50 per cent) of those are able to form stars. At z ∼ 8 the total $\dot{M}_\star/M_{gas}$ ratio for haloes with $M_{halo} = 10^{9-10}$ $M_\odot$ is high ($\dot{M}_\star/M_{gas} \sim 1.3 \times 10^{-10}$ yr^{-1}), while combined they contain ∼40 per cent of the total gas present in haloes in the simulation. Objects with masses around the Milky Way $M_{halo} = 10^{11-12}$ $M_\odot$ are more efficient by almost an order of magnitude but have significantly lower counts. Thus, low-mass haloes through their large numbers and low SFRs (Fig. 6) dominate the cosmic budget of star formation at this era. Up to z ∼ 5 the number of low-mass haloes is slowly increasing but a lot of them are merging to form larger structures. However, at this epoch only 20 per cent of them are able to form stars, and their efficiency ($\dot{M}_\star/M_{gas} \sim 4.2 \times 10^{-11}$ yr^{-1}) is significantly lower than in the past. In the following paragraphs we will see that at this era higher mass haloes ($M_{halo} = 10^{11-12}$ $M_\odot$) dominate the CSFRD. From z ∼ 5 to z ∼ 1 the total number of haloes with masses $M_{halo} = 10^{9-10}$ $M_\odot$ slightly increases, while from z ∼ 1 to z ∼ 0 it is kept almost constant (Warren et al. 2006; Lukić et al. 2007). At z ∼ 0 only 0.6 per cent of them are able to form stars, with their efficiency being only $\dot{M}_\star/M_{gas} \sim 6.6 \times 10^{-12}$ yr^{-1}. Their contribution to the cosmic budget is almost negligible (Fig. 4).

In Fig. 4 we see that at z ≥ 5 the contribution of large haloes ($M_{halo} \geq 10^{12}$ $M_\odot$) to the total SFR of the Universe is negligible. The left-hand panel of Fig. 5 reveals that the number density of these objects is small compared to low-mass haloes, which at this era dominate the Universe. However, haloes grow rapidly at high redshifts.[6] Mergers play an important role in the creation of large haloes in overdense regions, while diffuse accretion dominates the growth in voids. Fakhouri & Ma (2008) and Fakhouri, Ma & Boylan-Kolchin (2010) using the Millennium Simulations demonstrated that the rate of mergers increases with mass as ∝$M^{1.1}$ and with redshift as ∝$(1 + z)^{2.5}$. In addition, Qu et al. (2017) demonstrated that the merger fraction (the fraction of massive galaxies that are merging with a less massive companion) in the EAGLE simulation is large at higher redshifts, a behaviour that is broadly consistent with observations (Man, Zirm & Toft 2016). The left-hand panel of Fig. 5 reveals that the number density of haloes with masses $M_{halo} = 10^{11-12}$ $M_\odot$ has been increasing at high rate at z ∼ 5–8 in the L100N1504-Ref

---

[5] Haloes with masses $M_{halo} \leq 10^9$ $M_\odot$ contain less than 100 dark matter particles. In this regime sampling effects associated with the limited resolution become important (Katsianis, Tescari & Wyithe 2015) so we do not focus on objects that have masses less than $M_{halo} \leq 10^9$ $M_\odot$. We note that the exclusions of objects with masses $M_{halo} = 10^{7-9}$ $M_\odot$ from our discussion would not have an effect in our conclusions as the CSFRD and SFRF are dominated by more massive haloes (Figs 4 and 6).

[6] Correa et al. (2015) proposed that the total mass growth rate of a halo can be approximated by $\dot{M}_{tot} = 71.6$ $M_\odot$ yr^{-1} $(\frac{M(z)}{10^{12} \, M_\odot})(\frac{h}{0.7}) f(M_o)$

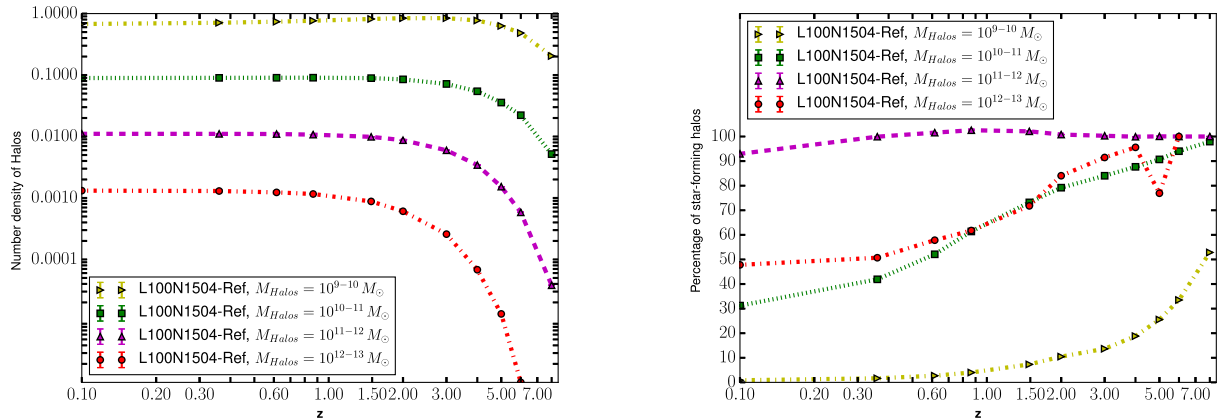$[(1 + z) - \alpha][\Omega_m(1 + z)^3]$.

Figure 5. Left-hand panel: evolution of the number of haloes with different masses in the L100N1504-Ref. Haloes with low masses are numerous even at high redshift while higher mass objects (e.g. $M_{\rm halo} \sim 10^{11-13}$ M$_\odot$) form with high rate up to redshift $z \sim 1.5$. Right-hand panel: percentage of star-forming haloes at different masses. Haloes with $M_{\rm halo} \sim 10^{11-12}$ M$_\odot$ are typically star forming at all redshift.
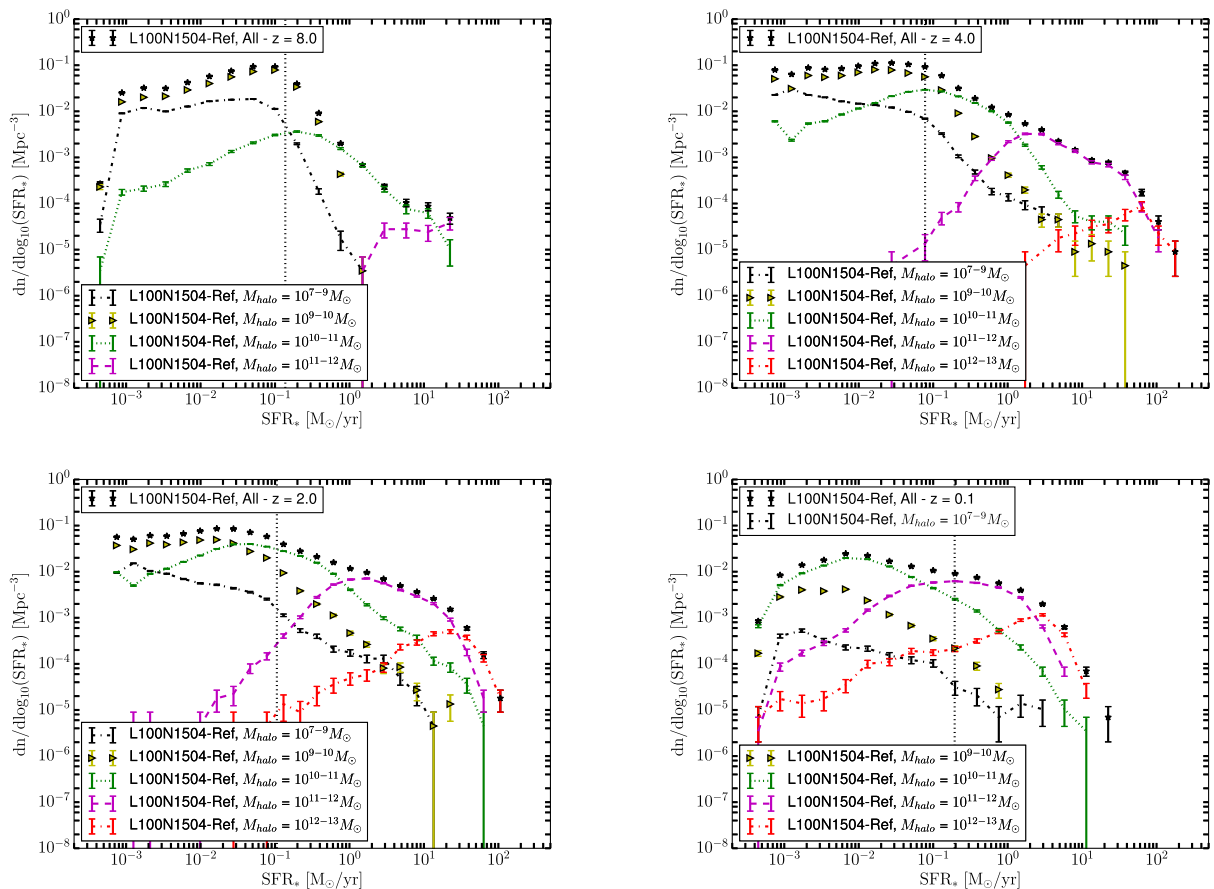

Figure 6. The contribution of dark matter haloes to the SFRF (black stars) for redshifts $z \sim 8.0$ (top left-hand panel), $z \sim 4.0$ (top right-hand panel), $z \sim 2.0$ (bottom left-hand panel) and $z \sim 0.1$ (bottom right-hand panel). Galaxies with SFR ≥ 1 M$_\odot$ yr^{-1} reside in large haloes $M_{\rm halo} \sim 10^{11-12}$ M$_\odot$ even at $z \sim 4.0$. These haloes represent only ~ 1 per cent of the total star-forming population at this era. In the local Universe the number of massive haloes $M_{\rm halo} \geq 10^{11}$ M$_\odot$ is significantly higher than that of $z \sim 4$. They dominate almost entirely the SFRF at SFR ≥ 0.1 M$_\odot$ yr^{-1}.

run. To indicate this we note that in only 0.5 Gyr, the number of haloes in this mass regime has increased by more than ~ 50 times. Starting from redshift $z \sim 5$ there is a sudden and immense increase in the contribution of $M_{\rm halo} \geq 10^{11}$ M$_\odot$ to the CSFRD. We note that the objects with $M_{\rm halo} = 10^{11-12}$ M$_\odot$ represent less than ~ 1 per cent of the total star-forming population at $z \sim 5$ (Fig. 5), they contain

only ~ 8 per cent of the total gas present in haloes, yet they are so successful at forming stars ($\dot{M}_\star/M_{\rm gas} \sim 4.2 \times 10^{-10}$ yr^{-1}) with respect to other haloes that they dominate the total CSFRD below $z < 5$. At $z \sim 2$–4 the number of haloes with $M_{\rm halo} = 10^{11-12}$ M$_\odot$ keeps increasing but at a relatively slower rate. By redshift ~ 1 most of the high-mass haloes ($M_{\rm halo} = 10^{11-13}$ M$_\odot$) have already

been formed in the EAGLE L100N1504-Ref something that is in agreement with the prediction from *N*-body simulations (Diemand, Kuhlen & Madau 2007). From redshift $z \sim 2$ to $z \sim 0$ the numbers of $M_{\mathrm{halo}} = 10^{11-12}\,\mathrm{M}_\odot$ and $M_{\mathrm{halo}} = 10^{12-13}\,\mathrm{M}_\odot$ haloes remain almost constant. At $z \sim 0$ objects with $M_{\mathrm{halo}} = 10^{11-12}\,\mathrm{M}_\odot$ represent almost ∼20 per cent of the total star-forming population and contain only ∼6 per cent of the total gas present in haloes in the simulation. Haloes of this mass interval have been dominating the CSFRD in the EAGLE simulation for more than 11 billion years through their high efficiencies.

It is important to see the contribution of haloes with different masses to the SFRF since different mechanisms that affect the SFRs of galaxies are related to the masses of their host haloes. In Fig. 6 we present the contribution of dark matter haloes to the SFRF (black stars) for redshifts $z \sim 8.0$ (top left-hand panel), $z \sim 4.0$ (top right-hand panel), $z \sim 2.0$ (bottom left-hand panel) and $z \sim 0.1$ (bottom right-hand panel). We see that typically at all times star forming efficient, high-mass haloes around $10^{12}\,\mathrm{M}_\odot$ completely dominate the SFRF at SFR $\geq 1.0\,\mathrm{M}_\odot\,\mathrm{yr}^{-1}$. As discussed in the previous paragraphs the growth of haloes is rapid at high redshifts. At $z \sim 4.0$ we see that galaxies with SFR $\geq 1\,\mathrm{M}_\odot\,\mathrm{yr}^{-1}$ reside entirely in large haloes at the mass regime of $M_{\mathrm{halo}} \sim 10^{11-13}\,\mathrm{M}_\odot$. Going to lower redshifts these objects make their dominance more absolute not only at the high star-forming rate end but to the whole distribution of SFRs. At $z \sim 2$ we see that the high star-forming galaxies SFR ~ 10–$100\,\mathrm{M}_\odot\,\mathrm{yr}^{-1}$ that contribute significantly to the peak of the CSFRD (see Section 4.2) mostly reside in haloes of mass $M_{\mathrm{halo}} \sim 10^{12-13}\,\mathrm{M}_\odot$, where AGN feedback can play a central role. We will see in detail in Section 6.2 the effect of the AGN feedback implementation used by EAGLE for these objects. Finally, at $z \sim 0$ we see that any galaxy with SFR $\geq 0.1\,\mathrm{M}_\odot\,\mathrm{yr}^{-1}$ resides entirely in large haloes with $M_{\mathrm{halo}} \sim 10^{11-13}\,\mathrm{M}_\odot$.

6 THE EFFECT OF FEEDBACK PRESCRIPTIONS ON THE STAR FORMATION RATE FUNCTION

6.1 The effect of the SN feedback on the star formation rate function

In Λ cold dark matter (ΛCDM) simulations there is a tendency for the gas in galaxies to transform into stars too efficiently and too early. As a result, the stellar mass fractions of simulated objects are larger with older stellar populations than those implied by observations (White & Frenk 1991; Guo et al. 2010; Moster et al. 2013). There has been a large effort in the last decades to find and understand mechanisms that can decrease this discrepancy. One such mechanism is stellar feedback.

Currently, simulations of large scales lack the resolution necessary to model the self-consistent development of outflows from feedback and rely on subgrid models. The most widely used types of prescriptions in the literature are:

(i) injecting energy in kinetic form (i.e. Springel & Hernquist 2003; Dalla Vecchia & Schaye 2008);

(ii) decoupling wind particles from hydrodynamical forces (i.e. Oppenheimer & Davé 2006; Tescari et al. 2014);

(iii) turning off radiative cooling and decoupling different thermal phases (i.e. Scannapieco et al. 2006);

(iv) thermal feedback (i.e. Stinson et al. 2006).

The EAGLE simulations adopt the stochastic thermal feedback scheme described in Dalla Vecchia & Schaye (2012). In addition to

the effect of reheating interstellar gas from star formation, which is already accounted in by the equation of state, galactic winds produced by Type II SNe are also considered following the implementation described below.[7] When a stellar particle has reached the age 3×10^7 yr, which corresponds to the maximum lifetime of a star that explodes as core-collapse SNe, it injects thermal energy to its neighbouring elements, increasing their internal energy and giving them a temperature jump ΔT. The total available energy per unit stellar mass provided by Type II SN, $\epsilon_{\mathrm{SNII}} = n_{\mathrm{SNII}} E_{\mathrm{SNII}}$, is described by

$$\epsilon_{\mathrm{SNII}} = 8.73 \times 10^{15}\,\mathrm{erg\,g^{-1}} \left(\frac{n_{\mathrm{SNII}}}{1.736 \times 10^{-2}\,\mathrm{M}_\odot^{-1}} \right) E_{51}, \qquad (10)$$

where E_{SNII} is the available energy from a single SNII, E_{51} a value that is related to the energy released by a single Type II SNe and n_{SNII} is their number. Therefore, the amount of energy available in an SSP particle is $m_\star \epsilon_{\mathrm{SNII}}$, where $m_\star$ is the mass of the star particle. To obtain the E_{51} and n_{SNII} in the simulation, the feedback from Type II SNe is subject to the two following assumptions:

(i) 6–100 $\mathrm{M}_\odot$ stars are the progenitors of Type II SNe;

(ii) each SN releases 10^{51} erg (i.e. $E_{\mathrm{SNII}} = 10^{51}$ erg and $E_{51} = 1$).

In the feedback scheme employed by EAGLE a fraction of the energy given by equation (10), f_{th}, is used. Implementing the density and metallicity requirements described in Schaye et al. (2015) to the functional form of f_{th}, the efficiency adopted in the simulations is written as

$$f_{\mathrm{th}} = f_{\mathrm{th,min}} + \frac{f_{\mathrm{th,max}} - f_{\mathrm{th,min}}}{1 + \left(\frac{Z}{0.1\,\mathrm{Z}_\odot} \right)^{n_Z} \left(\frac{n_{\mathrm{H,birth}}}{n_{\mathrm{H,0}}} \right)^{-n_n}}, \qquad (11)$$

where $n_{\mathrm{H,birth}}$ is the density of a gas particle at the instant it is converted into a star particle, $n_{\mathrm{H,0}} = 0.67\,\mathrm{cm}^{-3}$ set after comparing test simulations to the observed present-day galaxy stellar mass function (GSMF) and galaxy sizes, $\mathrm{Z}_\odot = 0.0127$ the solar metallicity, $n_z = n_n = 2/\ln 10$, $f_{\mathrm{th,min}} = 0.3$ and $f_{\mathrm{th,max}} = 3$. The maximum value $f_{\mathrm{th,max}}$ is achieved at low metallicities and high densities and vice versa.[8]

Fig. 7 shows the effect of scaling the f_{th} function and thus the feedback efficiency adopted by the Ref model (L25N376-Ref, dashed green line) by factors of 0.5 (L25N376-WeakSNfb, red dotted line) and 2 (L25N376-StrongSNfb, black solid line) on the SFRF at redshifts $z = 8.0$ (top left-hand panel), $z = 6.0$ (top right-hand panel), $z = 4.0$ (middle left-hand panel), $z = 2.0$ (middle right-hand panel), $z = 0.85$ (bottom left-hand panel) and $z = 0$ (bottom right-hand panel).[9] The asymptotic efficiencies of these models are

---

[7] The feedback prescription used in EAGLE does not distinguish Type II from Type Ib/c SNe. The physics of the later is not well understood so any event of core-collapse SNe is considered to follow the physics of Type II incidents.

[8] Values of f_{th} greater than unity are physically motivated by appealing to other sources of energy than SNe, e.g. stellar winds, radiation pressure, cosmic rays, or if SNe yield more energy per unit mass than initially assumed. Another important motivation is the need to deal with the finite numerical resolution of the simulations.

[9] The runs L25N376-Ref, L25N376-WeakSNfb and L25N376-StrongSNfb were performed in a small volume of 25 Mpc and an intermediate resolution same with L100N1504-Ref was employed. This volume is small to sample high star-forming objects. However, we demonstrate in Appendix B that if the resolution is kept the same, simulations with the same physics but different volumes produce SFRFs with the same shape, even for relatively high star-forming objects.
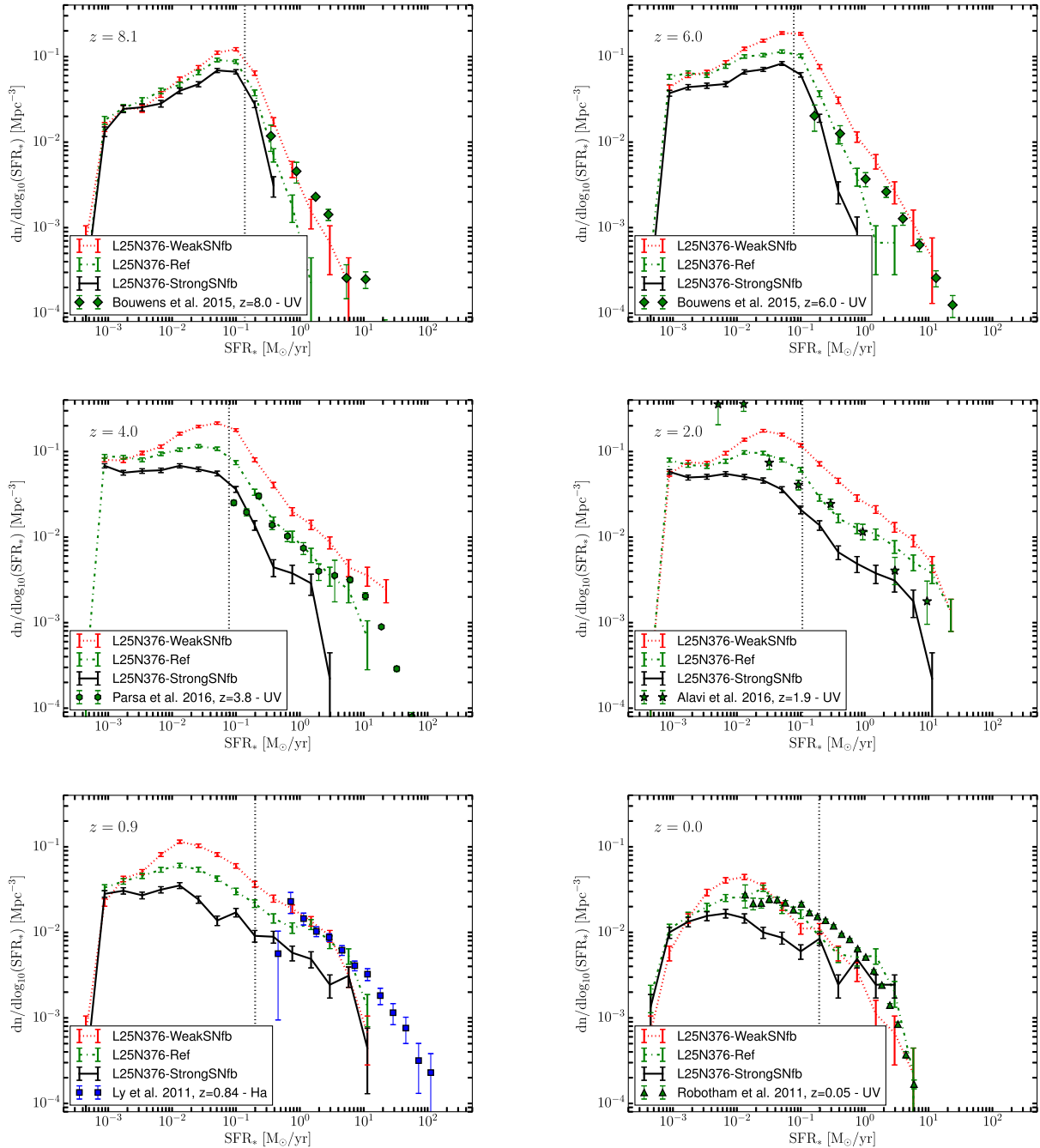
Figure 7. We present the effect of the SN feedback prescription used in the EAGLE-Ref simulation on the SFRF at $z \sim 0$–8. At redshifts $z \geq 2.0$ SN feedback decrease effectively the number of intermediate and high star-forming galaxies. At redshift $z \sim 0$ the SN feedback is less efficient at decreasing the SFR of highly star-forming systems. The agreement between the three configurations for objects SFR $\leq 0.1\,\mathrm{M_\odot\,yr^{-1}}$ is probably due to the fact that feedback is not resolved at these small galaxies.

$f_{\mathrm{th}}^{\min} = (0.15, 0.6)$ and $f_{\mathrm{th}}^{\max} = (1.5, 6.0)$, respectively. Galaxies in the EAGLE simulations start with high gas fractions and initially form stars too efficiently like in any other ΛCDM scenario so a feedback prescription is required to be efficient at these epochs. This can be achieved by employing a high $f_{\mathrm{th,\,max}}$ for the subgrid SNe feedback. In addition, since metallicity decreases with increasing redshift at a fixed stellar mass, the metallicity dependence on f_{th} described by equation (11) implies a feedback prescription that is

relatively more efficient at high redshifts (Schaye et al. 2015). However, at $z \sim 8.0$ the effect of the feedback prescription on the SFRF is not strong enough, possibly due to the fact that most of the objects are not resolved properly (see Section 4.1 for more details). On the other hand, at redshift 6 we see that the difference by a factor of 2 in f_{th} affect significantly the SFRF. The number of galaxies of intermediate star-forming objects (SFR ~ 1–$10\,\mathrm{M_\odot\,yr^{-1}}$) is affected almost by the same factor. We note that the run with weak feedback

is closer to the observations but the three different configurations we study have issues of resolution that play a major role at these high redshifts at the faint end of the distribution (the resolution employed is the same as the L100N1504-Ref). At redshifts $z \sim 4.0$ and $z \sim 2.0$ the reference model is in good agreement with observations while the simulation with two times lower f_{th} has an abundance of galaxies with intermediate (SFR ~ 1–$10\,M_\odot\,yr^{-1}$) and low SFRs (SFR ~ 1–$10\,M_\odot\,yr^{-1}$) larger by a factor of ~ 3. Thus, a small variation in the efficiency of feedback can affect the SFR by a large factor at epochs close to the peak of the CSFRD. However, going to lower redshifts we see that the change of f_{th} by the factor of 2 affects the SFRF only by ~ 1.5. Crain et al. (2015) presented the GSMF at $z \sim 0.1$ and demonstrated that a lower (higher) star formation feedback efficiency corresponds to a greater (smaller) abundance of galaxies with masses below the characteristic mass of the Schechter (1976) form (i.e. the SNe feedback prescription affects the low-mass end of the distribution) almost by a factor of 3. The SFRF at $z \sim 0$ is not affected significantly from changes to the f_{th}, thus the difference in the stellar masses between the three different configurations reported by Crain et al. (2015) for present day galaxies can be attributed mostly to the effects of SNe feedback at higher redshifts.

We find that SNe feedback is important at all redshifts and plays a major part for replicating the observed SFRFs at all epochs. However, we note that this prescription plays an increasing role at decreasing the SFRs of galaxies with redshift and especially at epochs close to the peak of the CSFRD. In addition, we demonstrated that the SN feedback mechanism employed by EAGLE affects the simulated objects similarly over the entire SFR range. This is in accordance with the findings of Katsianis et al. (2017) where the authors demonstrated that SN feedback prescriptions in cosmological hydrodynamic simulations need to play a major role at changing the abundances of low, intermediate and high star-forming galaxies at $z \sim 1$–4 and not only the low star-forming objects to match observations.

6.2 The effect of AGN feedback on the star formation rate function

Since AGN feedback quenches star formation in massive galaxies and regulates the growth of BHs, implementing a feedback prescription associated with SMBHs in cosmological simulations is essential to reproduce a range of observables like the high-mass end of the stellar mass function (Furlong et al. 2015) and BH masses (Rosas-Guevara et al. 2016). The method that EAGLE employs to seed galaxies with BHs is described by Springel (2005), where seed BHs are placed at the centre of every halo more massive than $10^{10}\,M_\odot/h$ that does not already contain a BH. When a seed is needed to be implemented at a halo, its highest density gas particle is converted into a collisionless BH particle inheriting the particle mass. These BHs grow by accretion of nearby gas particles or through mergers. The gas accretion obeys the Bondi–Hoyle–Lyttleton formula:

$$\dot{m}_{Bondi} = \frac{4\pi\,G^2\,m_{BH}^2\,\rho}{(c_s^2 + u^2)^{3/2}}, \tag{12}$$

where u the relative velocity of the BH and the gas, c_s the sound speed and ρ the density of the gas. EAGLE takes into account gas circulation to calculate a revised Bondi rate $\dot{m}_{Bondi,circ}$, which can be written as

$$\dot{m}_{Bondi,circ} = \dot{m}_{Bondi} \times min(C_{visc}^{-1}(c_s/V_\phi)^3, 1), \tag{13}$$

where $\dot{m}_{Bondi}$ is the Bondi & Hoyle (1944) rate applicable to spherically symmetric accretion (equation 12), V_Φ is the circulation speed of the gas around the BH computed using equation (16) of Rosas-Guevara et al. (2015) and C_{visc} is a free parameter related to the viscosity of a notional subgrid accretion disc. The accretion rate also cannot exceed the Eddington limit:

$$\dot{m}_{Edd} = \frac{4\pi G\,m_{BH}\,m_p}{\epsilon_r \sigma_T\,c}, \tag{14}$$

where m_p is the proton mass, σ_T the Thomson cross-section, ϵ_r the radiative efficiency of the accretion disc and c the speed of light. Thus the final accretion rate can be written as

$$\dot{m}_{accr} = min(\dot{m}_{Bondi,circ}, \dot{m}_{Edd}). \tag{15}$$

If the radiation of the accretion disc is taken into account, the growth of the BH can be written as

$$\dot{m}_{BH} = (1 - \epsilon_r)\,\dot{m}_{accr}. \tag{16}$$

EAGLE simulations assume a radiative efficiency of $\epsilon_r = 0.1$. Apart from accretion, BHs can grow via merging.

In the EAGLE simulations a single mode of AGN feedback is adopted in which energy is injected thermally and stochastically, in a similar way to energy feedback from star formation described in Section 6. The energy injection rate is specified as

$$\dot{E}_{AGN} = \epsilon_f\,\epsilon_r\,\dot{m}_{accr}\,c^2, \tag{17}$$

where ϵ_f is the fraction of the radiated energy that couples with the interstellar medium (ISM). Like in the case of feedback associated with star formation where f_{th} was specified, the value of ϵ_f must be chosen by calibrating the simulations to the observations. The parameter ϵ_f was calibrated by ensuring the normalization of the observed relation between BH mass and stellar mass is reproduced at $z = 0$ and set to $\epsilon_f = 0.15$ as in OWLS simulations. This implies that a fraction of $\epsilon_f \epsilon_r = 0.015$ of the accreted rest mass energy is returned to the local ISM.

In Fig. 8 we present the effect of the EAGLE AGN feedback prescription on the SFRF by comparing a run with AGN feedback (L50N752-Ref) and a simulation without (L50N752-NoAGN). Starting from redshift $z \sim 4$ we see that the two configurations have almost identical SFRFs in agreement with UV and IR constraints. The energy injection rate from a SMBH described by equation (17) shows a dependency with its accretion rate. The accretion rate is proportional to the mass of the BH and thus the AGN feedback prescription employed by EAGLE is dependent on the masses of the BHs. At high redshifts (e.g. $z \sim 4$) these do not have enough time to grow via mergers or accretion and hence the effect of the AGN feedback on the SFR of galaxies is negligible. However, going to $z \sim 2.0$ we see that the AGN feedback decreases the number density of highly star-forming objects (SFR ~ 10–$100\,M_\odot\,yr^{-1}$). We see that the reference model is in agreement with the UV constraints but the configuration without AGN feedback is actually in better agreement with the IR observations. The effect of the mechanism on the SFRF becomes more prominent at lower redshift and eventually at $z \sim 0$ the difference between the L50N752-Ref and L50N752-NoAGN runs can be even by a factor of 10 at the high end of the SFR range.

In Fig. 9 we present the evolution of the CSFRD of L50N752-Ref and L50N752-NoAGN runs at $z \sim 0$–8. At high redshifts $z \geq 4.0$ the two configurations are in agreement since AGN feedback is not effective yet. Going to lower redshifts we start seeing that the AGN feedback is responsible for decreasing the CSFRD significantly. In Section 4.2 we demonstrated that galaxies with
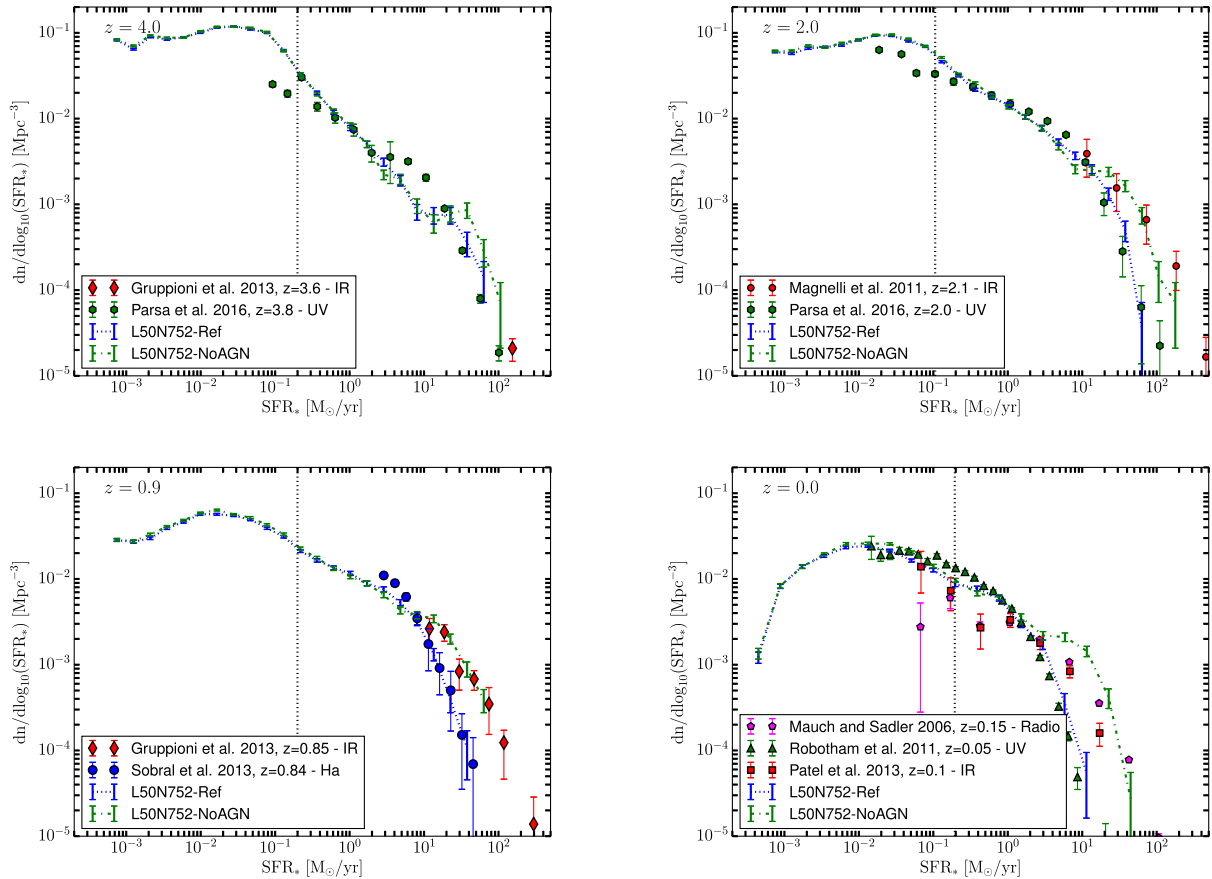
Figure 8. We present the effect of the AGN feedback prescription used in the EAGLE-Ref simulation on the SFRF at $z \sim 0$–4. Starting from intermediate redshifts ($z \sim 2$) the AGN feedback mechanism decreases the number of objects with high SFRs (SFR $\geq 10\,M_\odot\,\mathrm{yr}^{-1}$). The effect of the prescription becomes significant from intermediate redshifts and shape the high star-forming end at $z \leq 2$.
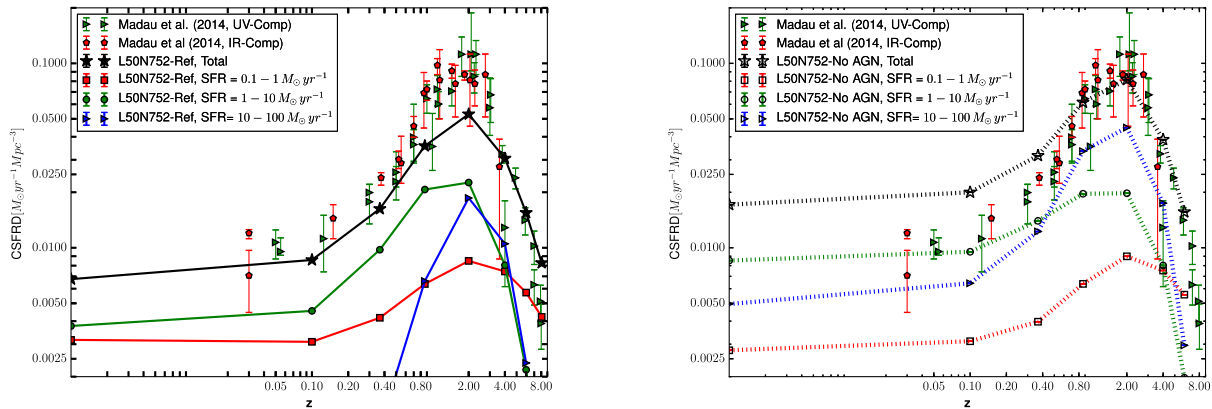

Figure 9. We present the effect of the EAGLE AGN feedback prescription on the CSFRD. We compare a run implemented with the AGN feedback mechanism (L50N752-Ref/left-hand panel) and a simulation without (L50N752-NoAGN/right-hand panel). AGN feedback makes its presence at $z < 3$ since it is proportional to the mass of the SMBHs in the simulation that increase with time. In the reference model the contribution of objects with SFR of 10–$100\,M_\odot\,\mathrm{yr}^{-1}$ is increasing at $z \sim 8$–2 but these galaxies are quenched by the AGN feedback. In the configuration without AGN feedback these objects continue to contribute significantly at $z < 2$ resulting in a CSFRD that is significantly higher than the constraints from observations.

SFR ~ 10–$100\,M_\odot\,\mathrm{yr}^{-1}$ contribute significantly at the CSFRD at its peak era. In the reference model, these are subject to the AGN feedback employed by EAGLE and from redshift $z \leq 2$ they significantly suppress any contribution to the cosmic budget. However, in the run where AGN feedback is not implemented (L50N752-NoAGN) galaxies with SFR ~ 10–$100\,M_\odot\,\mathrm{yr}^{-1}$ are not quenched

and they keep contributing significantly to the CSFRD at low and intermediate redshifts. We see that the peak of the CSFRD for the L50N752-NoAGN is 1.5 times higher than that of L50N752-Ref. The case without feedback is actually in better agreement with the compilation of UV, Hα and IR observations at $z \sim 2$. However, going to lower redshifts we see that the configuration without AGN

feedback has values ∼2.5 larger, which are significantly higher than observational constraints. The prescription is required as well to reproduce a range of observables, like the GSMF at $z \sim 0$. We have to note though, that AGN feedback is just a candidate for being the quenching mechanism that is necessary to decrease the mass and SFRs of high-mass galaxies at lower redshifts. It is possible that other physical mechanisms are involved to the quenching of high star-forming systems and maybe these could give a better match between observations and simulations at all redshifts for the CSFRD.

In conclusion, AGN feedback is crucial in EAGLE simulations for decreasing the number of highly star-forming systems below $z = 2$. The mechanism becomes more important with time since its effects are proportional to the masses of SMBHs that at high redshifts are small. We note that UV SFRF constraints are in agreement with the reference model but the IR observations are closer to the configuration without AGN feedback implementation. The prescription plays a major role for the peak value of the simulated CSFRD and regulates the cosmic budget of SFR at lower redshifts since it affects significantly the numbers of galaxies with SFR ∼ 10–100 $M_{\odot}$ yr^{-1} that have a large contribution if not quenched. This is in agreement with the results of van de Voort et al. (2011).

7 CONCLUSIONS AND DISCUSSION

In this paper, we investigated the evolution of the galaxy SFRF in the EAGLE simulations comparing the results to a compilation of UV, IR and Hα observations at $z \sim 0$–8. We present the constraints from various star formation tracers that can be used to constrain models and theory (for detailed tables see Appendix A and Katsianis et al. 2017). In addition, using cosmological hydrodynamic simulations we explored which haloes and what kind of objects dominate the CSFRD alongside with the importance of SNe and AGN feedback prescriptions. In the following we summarize the main results and conclusions of our analysis.

(i) There is a tension between the SFRFs of different indicators for high star-forming objects (SFR ∼ 10–100 $M_{\odot}$ yr^{-1}) at $0 \leq z \leq 2$ (Section 4.1). This discrepancy is more prominent with time and has its roots possibly in selection biases and the limitations of the different tracers. UV studies are possibly incomplete for the high star-forming systems, while IR data can give information only for dusty massive galaxies and are limited especially at high redshifts. UV and Hα light are subjects to dust attenuation effects and dust correction laws (e.g. IRX-β, 1 mag correction for the Hα) suggested in the literature may underestimate these. Thus, both tracers possibly underestimate the SFRF for high star-forming systems with high dust contents. On the other hand, IR light may overestimate the SFRs of galaxies due to various factors (e.g. the dust that it originates from can be heated by older stars, not related to newly born stars or AGN).

(ii) The SFRF of the EAGLE reference model is in good agreement with the constraints from UV and Hα observations at $z \sim 0$–8. IR and radio data typically suggest a higher number density of high star-forming systems compared to the above at $z \leq 2$ (Section 4.1). There is a slight underproduction of objects between 1 and 10 $M_{\odot}$ yr^{-1} in the reference model of EAGLE with respect the observed estimates, which may be due to the feedback implementations used. This small difference can be the origin of the offset between observed and simulated CSFRDs.

(iii) The CSFRD is dominated by galaxies with SFRs of 1–10 $M_{\odot}$ yr^{-1} at $z \leq 5$. Objects with lower SFRs do not contribute significantly to the cosmic budget at these redshifts, despite the fact that they are abundant (Section 4.2). The peak of the simulated CSFRD at $z \sim 2$ is partially driven by a large contribution of rare high star-forming galaxies (SFR ∼ 10–100 $M_{\odot}$ yr^{-1}). They decrease significantly and suddenly at $z \leq 0.8$ due to the presence of AGN feedback.

(iv) At $z \geq 5$ the CSFRD is mostly dominated by a large number of low-mass haloes ($M_{\rm halo} = 10^{9-10}\,M_{\odot}$) while the contribution from larger objects ($M_{\rm halo} \geq 10^{11}\,M_{\odot}$) is negligible (Section 5). However, haloes grow rapidly at high redshifts due to mergers and accretion. There is a sudden and significant increase in the numbers and contribution of haloes with masses $M_{\rm halo} = 10^{11-12}\,M_{\odot}$ to the CSFRD at $z \sim 5$. We note that galaxies that reside in haloes in this mass range represent less than the ∼1 per cent of the total population at $z \sim 5$ but still, these haloes are so efficient at forming stars that they dominate the total budget of cosmic star formation (Section 5). The above objects keep increasing in numbers at lower redshifts but at a relatively slower rate and their numbers are kept almost constant after $z \sim 2$, when the peak of the CSFRD is finally achieved. Haloes in the mass interval of $M_{\rm halo} = 10^{11-12}\,M_{\odot}$ have been dominating the CSFRD for most of the history of the Universe (i.e. most of the stars in the Universe, including ours, were born in Milky Way-like haloes).

(v) We find that SNe feedback is of great importance at all redshifts and plays a major part in replicating the observations at all epochs. We note that the prescription used by EAGLE plays an increasing role at decreasing the SFRs of galaxies at higher redshifts and especially at epochs close to the peak of the CSFRD (Section 6.1). We demonstrated that the mechanism affects the simulated objects similarly at all SFR regimes for $z \geq 1$ and not only at the faint end of the distribution.

(vi) AGN feedback is crucial for decreasing the number of high star-forming systems (SFR ∼ 10–100 $M_{\odot}$ yr^{-1}) and a thoughtful tuning is required to bring observations and simulations in agreement. The mechanism becomes prominent with time and plays a major role for the peak value of the simulated CSFRD since it affects the high star-forming systems that, if not quenched, can rise the cosmic budget of SFR at lower redshifts extensively (Section 6.2).

(vii) We require higher resolution simulations to make meaningful comparisons between the observed and simulated SFRFs at $z \geq 4$ for low star-forming objects. Even the EAGLE reference model L100N1504-Ref that is one of the state-of-the-art simulations in terms of resolution and volume is limited at high redshifts. In Appendix B, we perform resolution and box size tests and demonstrate that simulations with representative cosmological volumes (e.g. 25 or 50 Mpc) produce similar populations of galaxies in terms of SFR with configurations that employ significantly larger box sizes (e.g. 100 Mpc), provided that the resolution and subgrid physics are the same. Thus, for the study of SFRs of low and intermediate star-forming galaxies we suggest higher resolution cosmological hydrodynamic simulations run in representative volumes and a larger focus on subgrid physics. Larger volumes can be useful for the study of high star-forming systems and possibly can unravel the reasons for the tension between different SFR indicators.

REFERENCES

Alavi A. et al., 2016, ApJ, 832, 56
An F. X. et al., 2014, ApJ, 784, 152
Bauer A. E., Conselice C. J., Pérez-González P. G., Grützbauch R., Bluck A. F. L., Buitrago F., Mortlock A., 2011, MNRAS, 417, 289
Behroozi P. S., Wechsler R. H., Conroy C., 2013, ApJ, 770, 57
Bell E. F., Zheng X. Z., Papovich C., Borch A., Wolf C., Meisenheimer K., 2007, ApJ, 663, 834
Bondi H., Hoyle F., 1944, MNRAS, 104, 273
Bouwens R. J., Illingworth G. D., Franx M., Ford H., 2007, ApJ, 670, 928
Bouwens R. J. et al., 2011, ApJ, 737, 90
Bouwens R. J. et al., 2012, ApJ, 754, 83
Bouwens R. J. et al., 2015, ApJ, 803, 34
Bruzual G., Charlot S., 2003, MNRAS, 344, 1000
Chabrier G., 2003, PASP, 115, 763
Chang Y.-Y., van der Wel A., da Cunha E., Rix H.-W., 2015, ApJS, 219, 8
Correa C. A., Wyithe J. S. B., Schaye J., Duffy A. R., 2015, MNRAS, 450, 1514
Crain R. A. et al., 2009, MNRAS, 399, 1773
Crain R. A. et al., 2015, MNRAS, 450, 1937
Crain R. A. et al., 2017, MNRAS, 464, 4204
Cucciati O. et al., 2012, A&A, 539, A31
Dahlen T., Mobasher B., Dickinson M., Ferguson H. C., Giavalisco M., Kretchmer C., Ravindranath S., 2007, ApJ, 654, 172
Dalla Vecchia C., Schaye J., 2008, MNRAS, 387, 1431
Dalla Vecchia C., Schaye J., 2012, MNRAS, 426, 140
Davé R., Oppenheimer B. D., Finlator K., 2011, MNRAS, 415, 11
Davis M., Efstathiou G., Frenk C. S., White S. D. M., 1985, ApJ, 292, 371
Diemand J., Kuhlen M., Madau P., 2007, ApJ, 667, 859
Dolag K., Stasyszyn F., 2009, MNRAS, 398, 1678
Driver S. P., Robotham A. S. G., 2010, MNRAS, 407, 2131
Duncan K. et al., 2014, MNRAS, 444, 2960
Elbaz D. et al., 2010, A&A, 518, L29
Fakhouri O., Ma C.-P., 2008, MNRAS, 386, 577
Fakhouri O., Ma C.-P., Boylan-Kolchin M., 2010, MNRAS, 406, 2267
Fontanot F., Cristiani S., Santini P., Fontana A., Grazian A., Somerville R. S., 2012, MNRAS, 421, 241
Fumagalli M. et al., 2014, ApJ, 796, 35
Furlong M. et al., 2015, MNRAS, 450, 4486
Furlong M. et al., 2017, MNRAS, 465, 722
Gilbank D. G., Baldry I. K., Balogh M. L., Glazebrook K., Bower R. G., 2010, MNRAS, 405, 2594
Gruppioni C. et al., 2013, MNRAS, 432, 23
Gruppioni C. et al., 2015, MNRAS, 451, 3419
Guo Q., White S., Li C., Boylan-Kolchin M., 2010, MNRAS, 404, 1111
Hanish D. J. et al., 2006, ApJ, 649, 150
Hao C.-N., Kennicutt R. C., Johnson B. D., Calzetti D., Dale D. A., Moustakas J., 2011, ApJ, 741, 124

Hayward C. C. et al., 2014, MNRAS, 445, 1598
Henriques B. M. B., White S. D. M., Thomas P. A., Angulo R., Guo Q., Lemson G., Springel V., Overzier R., 2015, MNRAS, 451, 2663
Hirashita H., Buat V., Inoue A. K., 2003, A&A, 410, 83
Hopkins A. M., Connolly A. J., Haarsma D. B., Cram L. E., 2001, AJ, 122, 288
Jenkins A., 2013, MNRAS, 434, 2094
Karim A. et al., 2011, ApJ, 730, 61
Katsianis A., Tescari E., Wyithe J. S. B., 2015, MNRAS, 448, 3001
Katsianis A., Tescari E., Wyithe J. S. B., 2016, Publ. Astron. Soc. Aust., 33, e029
Katsianis A., Tescari E., Blanc G., Sargent M., 2017, MNRAS, 464, 4977
Kennicutt R. C., Jr, 1998a, ARA&A, 36, 189
Kennicutt R. C., Jr, 1998b, ApJ, 498, 541
Kennicutt R. C., Evans N. J., 2012, ARA&A, 50, 531
Lagos C. d. P. et al., 2015, MNRAS, 452, 3815
Lagos C. d. P., Theuns T., Stevens A. R. H., Cortese L., Padilla N. D., Davis T. A., Contreras S., Croton D., 2017, MNRAS, 464, 3850
Le Brun A. M. C., McCarthy I. G., Schaye J., Ponman T. J., 2014, MNRAS, 441, 1270
Lee J. C. et al., 2009, ApJ, 706, 599
Lewis G. F., Babul A., Katz N., Quinn T., Hernquist L., Weinberg D. H., 2000, ApJ, 536, 623
Lukić Z., Heitmann K., Habib S., Bashinsky S., Ricker P. M., 2007, ApJ, 671, 1160
Ly C., Lee J. C., Dale D. A., Momcheva I., Salim S., Staudaher S., Moore C. A., Finn R., 2011, ApJ, 726, 109
Madau P., Dickinson M., 2014, ARA&A, 52, 415
Magnelli B., Elbaz D., Chary R. R., Dickinson M., Le Borgne D., Frayer D. T., Willmer C. N. A., 2011, A&A, 528, A35
Magnelli B. et al., 2013, A&A, 553, A132
Man A. W. S., Zirm A. W., Toft S., 2016, ApJ, 830, 89
Marchetti L. et al., 2016, MNRAS, 456, 1999
Marigo P., 2001, A&A, 370, 194
Mauch T., Sadler E. M., 2007, MNRAS, 375, 931
Ménard B., Wild V., Nestor D., Quider A., Zibetti S., Rao S., Turnshek D., 2011, MNRAS, 417, 801
Meurer G. R., Heckman T. M., Calzetti D., 1999, ApJ, 521, 64
Monaco P., Fontanot F., Taffoni G., 2007, MNRAS, 375, 1189
Moster B. P., Naab T., White S. D. M., 2013, MNRAS, 428, 3121
Oppenheimer B. D., Davé R., 2006, MNRAS, 373, 1265
Otí-Floranes H., Mas-Hesse J. M., 2010, A&A, 511, A61
Papovich C., Finkelstein S. L., Ferguson H. C., Lotz J. M., Giavalisco M., 2011, MNRAS, 412, 1123
Parsa S., Dunlop J. S., McLure R. J., Mortlock A., 2016, MNRAS, 456, 3194
Patel H., Clements D. L., Vaccari M., Mortlock D. J., Rowan-Robinson M., Pérez-Fournon I., Afonso-Luis A., 2013, MNRAS, 428, 291
Planck Collaboration I, 2014, A&A, 571, A1
Planck Collaboration XVI, 2014, A&A, 571, A16
Portinari L., Chiosi C., Bressan A., 1998, A&A, 334, 505
Qu Y. et al., 2017, MNRAS, 464, 1659
Reddy N. A., Steidel C. C., 2009, ApJ, 692, 778
Reddy N. A., Steidel C. C., Pettini M., Adelberger K. L., Shapley A. E., Erb D. K., Dickinson M., 2008, ApJS, 175, 48
Robotham A. S. G. et al., 2011, MNRAS, 416, 2640
Rodighiero G. et al., 2010, A&A, 518, L25
Röllig M., Szczerba R., Ossenkopf V., Glück C., 2013, A&A, 549, A85
Rosas-Guevara Y. M. et al., 2015, MNRAS, 454, 1038
Rosas-Guevara Y., Bower R. G., Schaye J., McAlpine S., Dalla Vecchia C., Frenk C. S., Schaller M., Theuns T., 2016, MNRAS, 462, 190
Salpeter E. E., 1955, ApJ, 121, 161
Sanders D. B., Mazzarella J. M., Kim D.-C., Surace J. A., Soifer B. T., 2003, AJ, 126, 1607

Scannapieco C., Tissera P. B., White S. D. M., Springel V., 2006, MNRAS, 371, 1125

Schaye J., 2004, ApJ, 609, 667

Schaye J., Dalla Vecchia C., 2008, MNRAS, 383, 1210

Schaye J. et al., 2010, MNRAS, 402, 1536

Schaye J. et al., 2015, MNRAS, 446, 521

Schechter P., 1976, ApJ, 203, 297

Schiminovich D. et al., 2005, ApJ, 619, L47

Schmidt M., 1959, ApJ, 129, 243

Smit R., Bouwens R. J., Franx M., Illingworth G. D., Labbé I., Oesch P. A., van Dokkum P. G., 2012, ApJ, 756, 14

Sobral D., Smail I., Best P. N., Geach J. E., Matsuda Y., Stott J. P., Cirasuolo M., Kurk J., 2013, MNRAS, 428, 1128

Springel V., 2005, MNRAS, 364, 1105

Springel V., Hernquist L., 2003, MNRAS, 339, 289

Springel V., Yoshida N., White S. D. M., 2001, New Astron., 6, 79

Stinson G., Seth A., Katz N., Wadsley J., Governato F., Quinn T., 2006, MNRAS, 373, 1074

Sullivan M., Mobasher B., Chan B., Cram L., Ellis R., Treyer M., Hopkins A., 2001, ApJ, 558, 72

Takeuchi T. T., Yoshikawa K., Ishii T. T., 2003, ApJ, 587, L89

Tescari E., Katsianis A., Wyithe J. S. B., Dolag K., Tornatore L., Barai P., Viel M., Borgani S., 2014, MNRAS, 438, 3490

Trayford J. W. et al., 2015, MNRAS, 452, 2879

Utomo D., Kriek M., Labbé I., Conroy C., Fumagalli M., 2014, ApJ, 783, L30

van de Voort F., Schaye J., Booth C. M., Dalla Vecchia C., 2011, MNRAS, 415, 2782

Vogelsberger M., Genel S., Sijacki D., Torrey P., Springel V., Hernquist L., 2013, MNRAS, 436, 3031

Vogelsberger M. et al., 2014, MNRAS, 444, 1518

Warren M. S., Abazajian K., Holz D. E., Teodoro L., 2006, ApJ, 646, 881

White S. D. M., Frenk C. S., 1991, ApJ, 379, 52

Wiersma R. P. C., Schaye J., Theuns T., Dalla Vecchia C., Tornatore L., 2009, MNRAS, 399, 574

Wyder T. K. et al., 2005, ApJ, 619, L15

APPENDIX A: THE OBSERVED UV, IR AND Hα STAR FORMATION RATE FUNCTION

In this appendix we present the observed SFRF at $z \sim 0$–8, used for this work. The following tables are complimentary to those reported by Smit et al. (2012), Duncan et al. (2014) and Katsianis et al. (2017). Altogether, they give a description of the evolution of UV, IR and Hα SFRF functions for most of the history of the Universe. For the following estimations a Chabrier (2003) IMF and ΛCDM cosmology same with EAGLE were assumed. We note that an uncertainty of 50 per cent in the Kennicutt calibrations could lead to uncertainties for the estimates of the observed SFR by ∼0.3 dex.

Table A1. Stepwise SFR functions at $z \sim 5$–8 using the LFs from Bouwens et al. (2015, UV), equation (1) and the dust corrections described in Section 2.

$\frac{\text{SFR}}{\text{M}_\odot \, \text{yr}^{-1}}$	$dn/d\log_{10}(\phi_{\text{SFR}}) \, (\text{Mpc}^{-3}) \times 10^{-2}$
$z \sim 8.0$	UV dust corrected
43.269	0.0010 ± 0.0006
21.704	0.0026 ± 0.0010
10.891	0.0116 ± 0.0030
5.469	0.0120 ± 0.0050
2.850	0.0662 ± 0.0208
1.803	0.1066 ± 0.0452
0.902	0.2120 ± 0.0680
0.359	0.5480 ± 0.2080
$z \sim 7.0$	UV dust corrected
73.533	0.0002 ± 0.0004
41.186	0.0062 ± 0.0017
23.070	0.0090 ± 0.0028
12.921	0.0362 ± 0.0064
7.239	0.0578 ± 0.0114
4.235	0.1224 ± 0.0187
2.674	0.1697 ± 0.0331
1.687	0.3212 ± 0.0894
0.534	1.0925 ± 0.2731
0.171	1.5901 ± 0.5499
$z \sim 6.0$	UV dust corrected
141.748	0.0004 ± 0.0004
77.951	0.0028 ± 0.0012
42.862	0.0100 ± 0.0024
23.585	0.0330 ± 0.0047
12.974	0.0598 ± 0.0077
7.132	0.1305 ± 0.0015
3.921	0.2330 ± 0.0026
1.860	0.3554 ± 0.0598
0.742	1.2496 ± 0.2581
0.309	2.5517 ± 0.7857
$z \sim 5.0$	UV dust corrected
382.081	0.0004 ± 0.0004
208.215	0.0012 ± 0.0006
113.462	0.0063 ± 0.0015
61.828	0.0189 ± 0.0026
33.695	0.0495 ± 0.0047
18.369	0.1270 ± 0.0086
10.001	0.1925 ± 0.0125
5.452	0.2486 ± 0.0175
2.974	0.3900 ± 0.0319
1.280	0.8343 ± 0.0101
0.512	1.6080 ± 0.0331
0.203	4.5640 ± 0.0133

Table A2. Stepwise SFR functions at $z \sim 1.3$–2.6 using the LFs from Alavi et al. (2016, UV), equation (1) and the dust corrections described in Section 2.

$\dfrac{\text{SFR}}{\text{M}_\odot\,\text{yr}^{-1}}$	$\mathrm{d}n/\mathrm{d}\log_{10}(\phi_{\text{SFR}})\,(\text{Mpc}^{-3})\times 10^{-2}$
$z \sim 2.6$	UV dust corrected
11.662	$0.2020\pm^{0.1216}_{0.0804}$
3.214	$0.4714\pm^{0.1627}_{0.1235}$
0.881	$0.9121\pm^{0.2113}_{0.1739}$
0.259	$2.2186\pm^{0.2843}_{0.2843}$
0.938	$4.0594\pm^{0.4957}_{0.4957}$
0.371	$13.1310\pm^{1.7996}_{1.7996}$
0.015	$39.1263\pm^{10.5453}_{8.4968}$
0.006	$19.2142\pm^{25.3427}_{12.4122}$
$z \sim 1.9$	UV dust corrected
10.337	$0.1777\pm^{0.1197}_{0.0767}$
3.259	$0.4059\pm^{0.1627}_{0.1197}$
1.024	$1.1150\pm^{0.2451}_{0.2057}$
0.325	$2.4450\pm^{0.3105}_{0.3105}$
0.102	$4.0894\pm^{0.4920}_{0.4920}$
0.035	$7.4155\pm^{1.3675}_{1.1673}$
0.014	$35.9610\pm^{7.1612}_{6.0518}$
0.006	$35.7384\pm^{21.3488}_{14.1764}$
$z \sim 1.3$	UV dust corrected
13.599	$0.1291\pm^{0.0767}_{0.0505}$
4.266	$0.5986\pm^{0.1484}_{0.1141}$
1.339	$0.9166\pm^{0.1664}_{0.1421}$
0.420	$1.0158\pm^{0.1852}_{0.1571}$
0.132	$1.1990\pm^{0.2563}_{0.2562}$
0.041	$4.2391\pm^{0.5761}_{0.5761}$
0.014	$15.4802\pm^{3.5113}_{2.9711}$
0.006	$39.8072\pm^{14.3915}_{10.8988}$

Table A3. Stepwise SFR functions at $z \sim 0.4$ using the LFs from Sobral et al. (2013, Hα) and equation (3).

$\dfrac{\text{SFR}}{\text{M}_\odot\,\text{yr}^{-1}}$	$\mathrm{d}n/\mathrm{d}\log_{10}(\phi_{\text{SFR}})\,(\text{Mpc}^{-3})\times 10^{-2}$
$z \sim 0.4$	Hα dust corrected (1 mag)
16.998	0.0182 ± 0.0157
8.513	0.0257 ± 0.0190
5.374	0.0873 ± 0.0516
4.271	0.1233 ± 0.0486
3.397	0.1742 ± 0.0603
2.695	0.1910 ± 0.0723
2.144	0.2518 ± 0.0696
1.709	0.3243 ± 0.0776
1.353	0.3556 ± 0.0782
1.071	0.4797 ± 0.0960
0.852	0.5023 ± 0.0903
0.684	0.7095 ± 0.1420
0.542	0.8729 ± 0.1389
0.435	1.0986 ± 0.1632
0.343	1.4487 ± 0.1277
0.276	1.4487 ± 0.1363
0.217	1.8663 ± 0.1756
0.171	2.0463 ± 0.1924

Table A4. Stepwise SFR functions at $z \sim 0.3$ and $z \sim 0.375$ using the LFs from Patel et al. (2013, IR) and Gruppioni et al. (2013, IR), respectively, and equation (2).

$\dfrac{\text{SFR}}{\text{M}_\odot\,\text{yr}^{-1}}$	$\mathrm{d}n/\mathrm{d}\log_{10}(\phi_{\text{SFR}})\,(\text{Mpc}^{-3})\times 10^{-2}$
$z \sim 0.3$	IR
116.953	$0.0017\pm^{0.0007}_{0.0018}$
46.564	$0.0129\pm^{0.0024}_{0.0030}$
18.541	$0.0760\pm^{0.0105}_{0.0105}$
7.382	$0.1742\pm^{0.0441}_{0.0602}$
2.948	$0.1025\pm^{0.0567}_{0.1512}$
$z \sim 0.375$	IR
205.554	0.0002 ± 0.0002
65.002	0.0048 ± 0.0011
20.557	0.0709 ± 0.0049
6.504	0.2143 ± 0.0197
2.061	0.3990 ± 0.1011

Table A5. Stepwise SFR functions at $z \sim 0.15$ using the LFs from Mauch & Sadler (2007, Radio) and the radio–SFR conversion law given by Sullivan et al. (2001).

$\dfrac{\text{SFR}}{\text{M}_\odot\,\text{yr}^{-1}}$	$\mathrm{d}n/\mathrm{d}\log_{10}(\phi_{\text{SFR}})\,(\text{Mpc}^{-3})\times 10^{-2}$
$z \sim 0.15$	Radio
267.179	$0.0002\pm^{0.0001}_{0.0001}$
106.363	$0.0009\pm^{0.0001}_{0.0001}$
42.345	$0.0077\pm^{0.0004}_{0.0004}$
16.866	$0.0356\pm^{0.0016}_{0.0016}$
6.711	$0.1073\pm^{0.0025}_{0.0025}$
2.671	$0.1954\pm^{0.0090}_{0.0090}$
1.063	$0.3096\pm^{0.0214}_{0.0214}$
0.423	$0.2824\pm^{0.0260}_{0.0325}$
0.169	$0.6038\pm^{0.1252}_{0.1530}$
0.067	$0.2759\pm^{0.1272}_{0.2470}$

Table A6. Stepwise SFR functions at $z \sim 0.1$ using the LFs from Patel et al. (2013, IR) and equation (2).

$\dfrac{\text{SFR}}{\text{M}_\odot\,\text{yr}^{-1}}$	$\mathrm{d}n/\mathrm{d}\log_{10}(\phi_{\text{SFR}})\,(\text{Mpc}^{-3})\times 10^{-2}$
$z \sim 0.1$	IR
271.705	0.0005 ± 0.0003
43.062	0.0003 ± 0.0005
17.143	0.0159 ± 0.0047
6.825	0.0837 ± 0.0135
2.717	0.1790 ± 0.0289
1.082	0.3334 ± 0.0614
0.431	0.2710 ± 0.1186
0.171	0.7293 ± 0.3025
0.068	1.3897 ± 0.7044

Table A7. Stepwise SFR functions at $z \sim 0.1$ using the LFs from Marchetti et al. (2016, IR) and equation (2).

$\frac{\text{SFR}}{\text{M}_\odot \ \text{yr}^{-1}}$	$\mathrm{d}n/\mathrm{d}\log_{10}(\phi_{\text{SFR}})\,(\text{Mpc}^{-3}) \times 10^{-2}$
$z \sim 0.06$	IR
15.634	0.0060 ± 0.0035
10.817	0.0100 ± 0.0045
7.313	0.0460 ± 0.0096
4.944	0.0764 ± 0.0123
3.343	0.1078 ± 0.0149
2.312	0.2773 ± 0.0242
1.563	0.3917 ± 0.0297
1.082	0.4931 ± 0.0392
0.731	0.6500 ± 0.0504
0.494	0.6652 ± 0.0897
0.334	0.5928 ± 0.0876
0.231	0.9145 ± 0.1790
0.156	0.6807 ± 0.1790
0.108	0.6965 ± 0.2202

Table A8. Stepwise SFR functions at $z \sim 0.05$ using the LFs from Robotham et al. (2011, UV), equation (1) and the dust corrections described in Section 2.

$\frac{\text{SFR}}{\text{M}_\odot \ \text{yr}^{-1}}$	$\mathrm{d}n/\mathrm{d}\log_{10}(\phi_{\text{SFR}})\,(\text{Mpc}^{-3}) \times 10^{-2}$
$z \sim 0.05$	UV dust corrected
20.611	0.0007 ± 0.0007
11.544	0.0004 ± 0.0004
8.640	0.0049 ± 0.0014
6.466	0.0147 ± 0.0017
4.839	0.0326 ± 0.0028
3.622	0.0740 ± 0.0042
2.711	0.1235 ± 0.0052
2.028	0.2118 ± 0.0070
1.518	0.3107 ± 0.0087
1.113	0.4507 ± 0.0112
0.850	0.5640 ± 0.0140
0.636	0.7246 ± 0.0186
0.476	0.8337 ± 0.0235
0.356	1.0438 ± 0.0312
0.267	1.2122 ± 0.0403
0.199	1.3437 ± 0.0484
0.149	1.4899 ± 0.0624
0.112	1.8835 ± 0.0863
0.084	1.6113 ± 0.1199
0.063	1.9389 ± 0.1210
0.047	2.1058 ± 0.1554
0.035	2.1441 ± 0.1884
0.026	1.9287 ± 0.2448
0.020	1.0907 ± 0.2999
0.015	2.4152 ± 0.7257

APPENDIX B: RESOLUTION AND BOX SIZE EFFECTS ON THE EAGLE STAR FORMATION RATE FUNCTION

In this appendix we present the resolution and box size effects on the SFRF. In Fig. B1 we compare the SFRFs of the L25N376-Ref, L50N752-Ref and L100N1504-Ref simulations. The three different runs employ the same subgrid parameters, feedback prescriptions and identical resolution. However, the box size is changed by a factor of 8 and 64 with respect the L25N376-Ref run. We see that the different configurations are in excellent agreement with
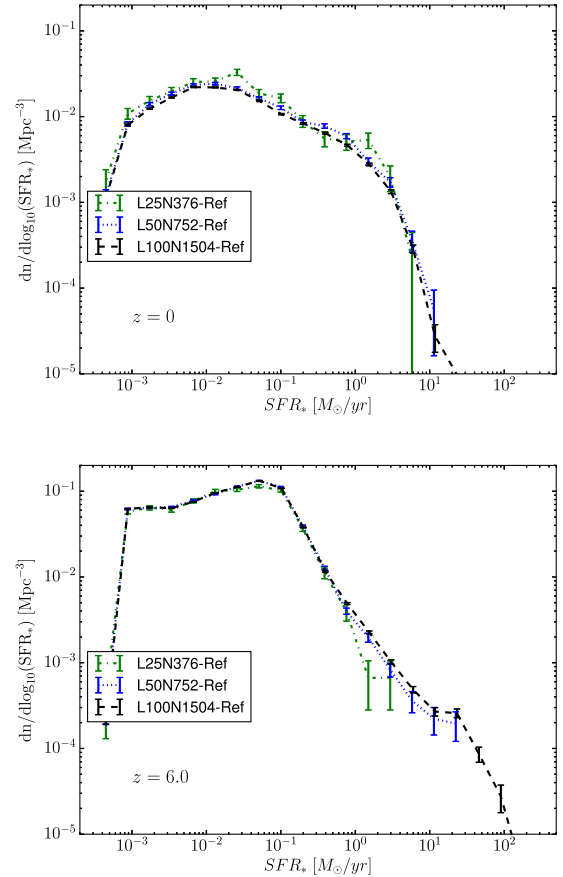
Figure B1. To illustrate convergence as the simulation volume is varied, the reference model at intermediate resolution is shown in volumes of $L = 25$, 50 and 100 Mpc boxes for redshifts $z \sim 0$ (top) and $z \sim 6$ (bottom). The two configurations with the largest volumes give better statistics at the high star-forming end, while the run with the smallest box size is unable to sample active galaxies with SFR $\geq 10\,\text{M}_\odot\,\text{yr}^{-1}$. Otherwise there are no differences besides the huge differences in box size.

each other and illustrate convergence as the simulation volume is varied both at redshifts $z = 0$ and $z = 6$. The largest volumes can give better statistics at the high star-forming end, while the simulation with the smallest box size considered is unable to sample active galaxies with SFR $\geq 10\,\text{M}_\odot\,\text{yr}^{-1}$. Otherwise there are no differences in the three distributions besides the huge differences in box size. The above, point to the direction that simulations with representative cosmological volumes (e.g. 25 Mpc) can produce similar populations of galaxies with state-of-the-art cosmological hydrodynamic simulations that employ significantly larger box sizes (e.g. 100 Mpc), provided that the resolutions and subgrid physics are similar (Katsianis et al. 2016).

In Fig. B2 we present a comparison between the L25N188-Ref, L25N376-Ref and L25N752-Ref runs to investigate the effect of changing the resolution in the EAGLE reference model. In the last two configurations the mass and spatial resolution differ by factors of 8 and 64, respectively, with regard the lowest resolution run L25N188-Ref. Schaye et al. (2015) and Crain et al. (2015) argued that hydrodynamical simulations such as EAGLE should recalibrate the efficiency of the subgrid feedback when the resolution is changed substantially since keeping the parameters the same does not guarantee that the physical models remain unchanged. In Section 6 we showed that the efficiencies of SNe and AGN feedback
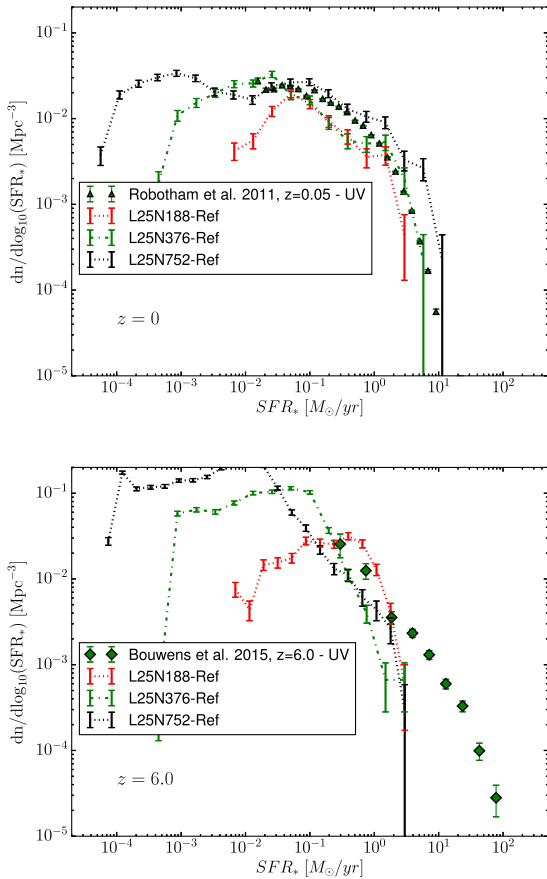
Figure B2. Resolution tests for redshifts $z \sim 0$ (top) and $z \sim 6$ (bottom) where the box size is kept fixed while the number of particles is varied. The mass and spatial resolution differ by factors of 8 and 64, respectively, for the L25N376 and L25N752, with regard the lowest resolution run L25N188-Ref. The simulated SFRFs do not converge, since the parameters for subgrid feedback are kept the same ('strong convergence test') besides the large differences in resolution. We perform a weak convergence test in Fig. B3.

are not predicted from first principles and are actually constrained from observations (e.g. GSMF at $z \sim 0$). Thus, in the case that the resolution changes substantially a recalibration is desired and that is the reason that L25N188-Ref, L25N376-Ref and L25N752-Ref runs may not converge.

Schaye et al. (2015) introduced the terminology of 'weak convergence' to describe the consistency of simulation outcomes in the case at which subgrid parameters are recalibrated when the resolution is changed, as opposed to the 'strong convergence' at which we hold the parameters fixed. To test if the simulations can fulfil the weak convergence test the L25N752-Recal simulation was run. In this simulation the following parameters for the feedback were changed with respect the reference model:

(i) temperature increment from the AGN $\Delta T_{\mathrm{AGN}} = 10^9$ K instead of $\Delta T_{\mathrm{AGN}} = 10^{8.5}$;[10]

(ii) subgrid BH viscosity parameter $C_{\mathrm{visc}} = 2\pi \times 10^3$ instead of $C_{\mathrm{visc}} = 2\pi$;[11]

(iii) $n_{\mathrm{H,\,0}} = 0.25\,\mathrm{cm}^{-3}$ instead of $n_{\mathrm{H,\,0}} = 0.67\,\mathrm{cm}^{-3}$ (equation 11);

(iv) power-law exponent for the density term $n_{\mathrm{n}} = 1/\ln 10$ instead of $n_{\mathrm{n}} = 2/\ln 10$.[12]

The parameters of the subgrid models for feedback from star formation and for gas accretion on to BHs were recalibrated in order to reproduce the observed $z \sim 0$ GSMF. In Fig. B3 we present the weak conversion test for the SFRF and compare the L25N752-Recal and L100N1504-Ref configurations for $z \sim 4$, $z \sim 2$, $z \sim 0.85$ and $z \sim 0$. Both runs are in agreement with observations and the weak convergence is fulfilled. However, the recalibrated model at redshift $z \sim 0$ overproduces the number density of objects with SFR ~ 1–$5\,\mathrm{M}_{\odot}\,\mathrm{yr}^{-1}$. The recalibration was performed to match the stellar mass function at $z \sim 0$ and this is reflected in the good convergence of L25N752-Recal and L100N1504-Ref at higher redshifts.

---

[10] Increasing the temperature increment helps to suppress the increase in the cooling losses that would otherwise occur due to the higher gas densities that are resolved in the higher resolution model. Without this change the AGN feedback would be insufficient effective.

[11] L25N752-Recal uses a different value for the parameter that controls the importance of angular momentum in suppressing accretion on to BHs, making the accretion rate more sensitive to the angular momentum of the accreting gas. Without this change, AGN feedback would become important at too low masses.

[12] The mean values of the efficiency of the SNe feedback, f_{th}, is almost the same in the Ref (1.07) and Recal models (1.06).
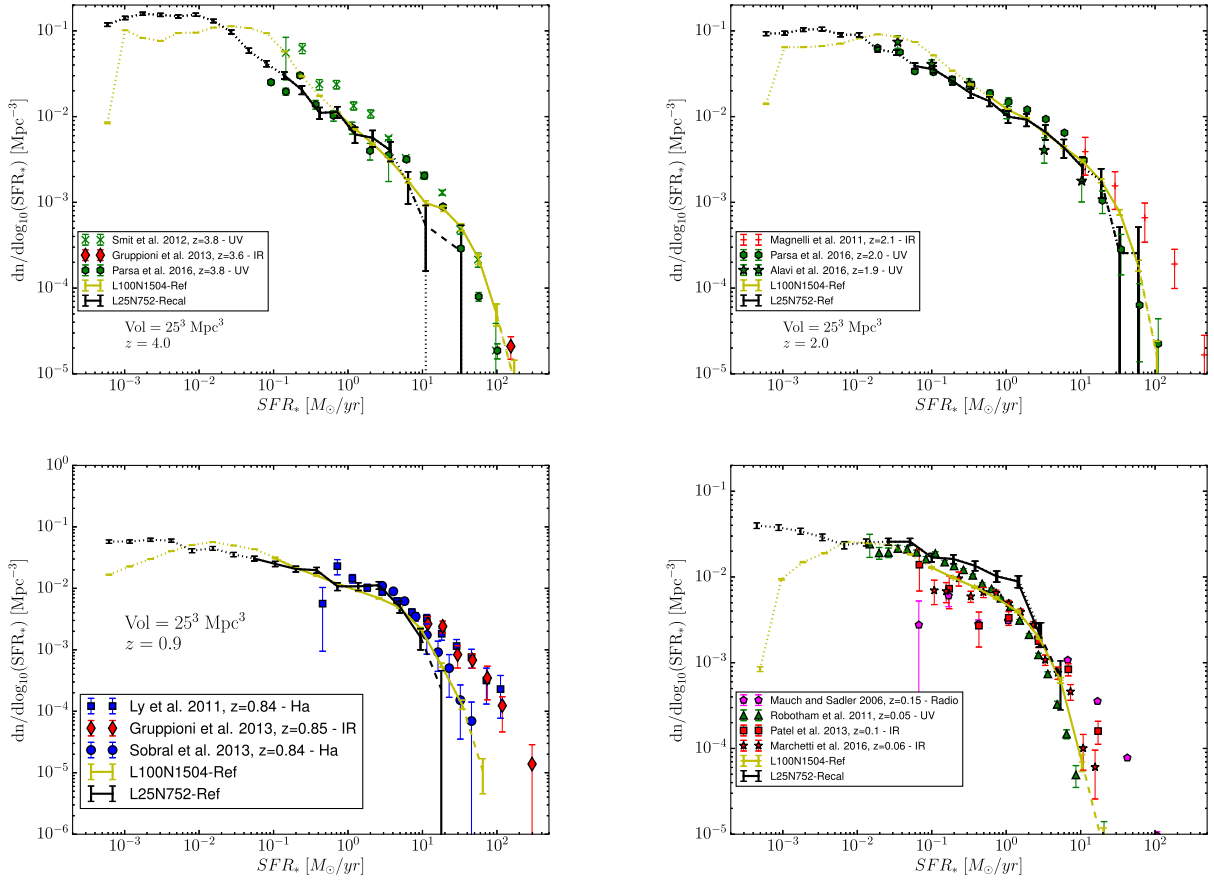
Figure B3. We present the weak convergence of the EAGLE simulated SFRF by comparing the L100N1504-Ref and L25N752-Recal runs at redshifts $z \sim 4$, $z \sim 2$, $z \sim 0.85$ and $z \sim 0$. The L25N752-Recal configuration has eight times higher resolution than the reference model so a recalibration of its subgrid physics is required to replicate the observed stellar mass function. When a bin of the EAGLE SFRF contains objects with stellar masses below the mass limit of 100 baryonic particles curves are dotted, when there are fewer than 10 galaxies curves are dashed.

This paper has been typeset from a TEX/LATEX file prepared by the author.